Accurate Force Fields for Atomistic Simulations of Oxides, Hydroxides, and Organic Hybrid Materials up to the Micrometer Scale

Krishan Kanhaiya,¹ Michael Nathanson,¹ Pieter J. in 't Veld,² Cheng Zhu,¹ Ilia Nikiforov,³ Ellad B. Tadmor,³ Yeol Kyo Choi,⁴ Wonpil Im,⁴ Ratan K. Mishra,² Hendrik Heinz^{1*}

¹ Department of Chemical and Biological Engineering, University of Colorado at Boulder, Boulder, CO 80309, USA

² BASF SE, Molecular Modeling & Drug Discovery, Carl Bosch Str. 38, 67056 Ludwigshafen,
Germany

³ Department of Aerospace Engineering and Mechanics, University of Minnesota, Minneapolis,

MN 55455, USA

* Corresponding author: hendrik.heinz@colorado.edu

⁴Department of Biological Sciences, Lehigh University, Bethlehem, Pennsylvania 18015, USA

Abstract

The simulation of metals, oxides, and hydroxides can accelerate the design of therapeutics, alloys, catalysts, cement-based materials, ceramics, bioinspired composites, and glasses. Here we introduce the INTERFACE force field (IFF) and surface models for α-Al₂O₃, α-Cr₂O₃, α-Fe₂O₃, NiO, CaO, MgO, β -Ca(OH)₂, β -Mg(OH)₂, and β -Ni(OH)₂. The force field parameters are nonbonded, including atomic charges for Coulomb interactions, Lennard-Jones (LJ) potentials for van-der-Waals interactions with 12-6 and 9-6 options, as well as a harmonic bond stretching for hydroxide ions. The models outperform DFT calculations and earlier atomistic models (Pedone, ReaxFF, UFF, CLAYFF) up to two orders of magnitude in reliability, compatibility, and interpretability due to a quantitative representation of chemical bonding consistent with other compounds across the periodic table and curated experimental data for validation. The IFF models exhibit average deviations of 0.2% in lattice parameters, <10% in surface energies (to the extent known), and 6% in bulk moduli relative to experiments. The parameters and models can be used with existing parameters for solvents, inorganic compounds, organic compounds, biomolecules, and polymers in IFF, CHARMM, CVFF, AMBER, OPLS-AA, PCFF, COMPASS, to simulate bulk oxides, hydroxides, electrolyte interfaces, multiphase, biological and organic hybrid materials at length scales from atoms to micrometers. The nonbonded character of the models also enables the analysis of mixed oxides, glasses, certain chemical reactions, and well-performing nonbonded models for silica phases, SiO2, are introduced. Automated model building is available in CHARMM-GUI Nanomaterial Modeler. We illustrate applications of the models to predict the structure of mixed oxides, energy barriers of ion migration, as well as binding energies of water and organic molecules in outstanding agreement with experimental data. Examples of model building for hydrated, pH-sensitive oxide surfaces to simulate solid-electrolyte interfaces are discussed.

Keywords: Interface Force Field, Bunsenite, Periclase, Quick Lime, Caustic Lime, Corundum, Eskolaite, Hematite, Silica, Oxides, Hydroxides, Atomistic Simulation, Molecular Dynamics, Atomic Charges

1. Introduction

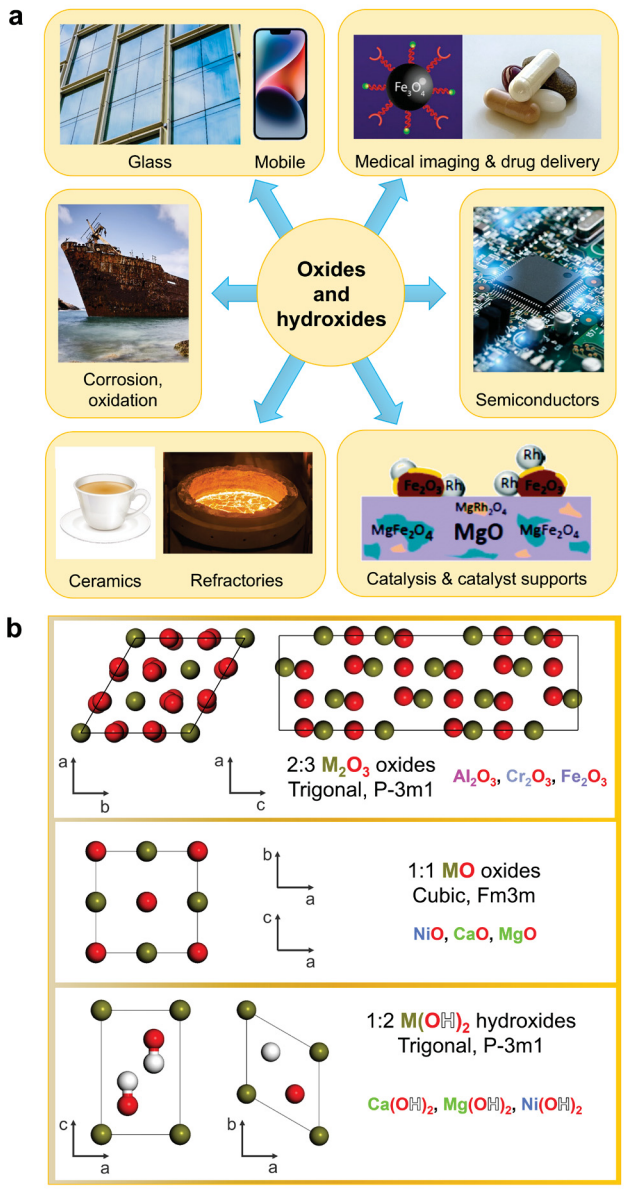
Oxides and hydroxides find widespread uses in structural and household applications, electronics, catalysis, and medicine (Figure 1a). For example, oxides are abundantly present in cement, ceramic, refractory, abrasive, and glass products, as well as in semi-conductors. ¹⁻³ Pure and mixed metal oxides serve as catalysts and catalyst supports to direct chemical reactions. ⁴ In the medical arena, surface-modified oxide and hydroxide nanoparticles are utilized for drug delivery and as antimicrobial agents. ^{5,6} Oxides further play an important role as thin films for corrosion protection on metals, or form undesired oxide/hydroxide scale as a result of corrosion. ^{7,8} Jewelry and ornaments often feature oxides, too, and have fascinated mankind from the earliest ages. ⁹

The structure of crystalline oxides and hydroxides is well known from X-ray and neutron scattering experiments. ¹⁰⁻¹⁶ The characterization of nanostructures, defects, metal-oxide-hydroxide interfaces, as well as their organic and biological modifications can be accomplished using various imaging techniques such as transmission electron microscopy, scanning tunneling electron microscopy, atomic force microscopy, X-ray photoelectron spectroscopy, electrochemical measurements, and surface analysis techniques. ¹⁷⁻¹⁹ However, laboratory studies rarely reach

atomic-level resolution. State-of-the-art atomic electron tomography (AET), for example, currently requires several years of effort to obtain all-atom 3D images of a limited number of noncrystalline nanostructures of 10³ to 10⁴ atoms, and the resolution is typically only high enough for metals, and not sufficient to locate oxygen atoms in oxides, carbon atoms in carbides, or organic matter.²⁰⁻²² Information in limited nanometer resolution can also be obtained from energydispersive X-ray spectroscopy (EDX).^{23, 24} Measurements of defect formation energies, the characterization of the chemistry of hydrated oxide surfaces, solid-electrolyte interactions, and the binding mechanisms of organic reactants and biological macromolecules such as proteins is also a great challenge, for example, due to the destructive nature of electron beams. Chemically realistic models and molecular dynamics simulations can fill in such gaps and provide acceleration using inputs from experiments and chemical knowledge, 25 such as X-ray data, knowledge of hydration reactions, data from surface titration experiments and pK values of acidic surface groups. The INTERFACE force field (IFF)²⁶ delivers accurate, compatible, and computationally efficient models, covering a wide range of metals, ^{27,28} minerals such as silica, ^{29,30} apatites, ³¹ clays, ³² cement minerals,^{33, 34} 2D materials,^{35, 36} and a few oxides.³⁷ In this contribution, we expand the coverage of IFF to chemically diverse oxides, hydroxides, mixed oxides, and their interfaces with electrolytes, organic, and biologically important molecules.

We introduce the IFF models for 9 common oxides and hydroxides, focusing on the development and validation of the all-atom models and potential applications. Our compounds include the three corundum-type oxides α -Al₂O₃, α -Cr₂O₃, α -Fe₂O₃, the three rock salt type oxides CaO, MgO and NiO, and the three hydroxides β -Ca(OH)₂, β -Mg(OH)₂ and β -Ni(OH)₂ (Figure 1b), as well as compatible nonbonded models for silica (discussed separately). Chemical bonding in these compounds is partly ionic and partly covalent. The amount of covalent and ionic character

in these compounds was determined from experimentally observed atomic charges of the constituent elements³⁸⁻⁴⁰ and the extended Born Model by Heinz et al. (Figure 1c).⁴¹ The extended Born model is of foundational importance to IFF and can be used to estimate atomic charges for compounds with similar chemistry and coordination numbers within $\pm 10\%$ reliability in relation to reference compounds with known atomic charges. The model evaluates the bond polarity and magnitude of atomic charges in a compound using the energy contributions of the individual steps that describe the formation from the elements in a thermodynamic cycle (Figure 1c, bottom). The individual steps involve the atomization energy, the ionization energy, the electron affinity, as well as electrostatic and covalent contributions to bonding. Higher atomization energies and higher ionization energies indicate stronger covalent bonding, equal to lower atomic charges. Reference information on atomic charges is available from experimentally determined deformation electron densities and dipole moments, 38-40 from validated IFF models for chemically similar minerals (silica, aluminates, calcium salts, metal sulfides), ^{26, 30, 42, 43} as well as the interpretation of atomic charges in the context of related physical and chemical properties of a group of related compounds. 41 The extended Born model, in combination with experimental data, fares an order of magnitude better than QM methods to assign atomic charges, which lead to >100% scatter and are not recommended for force field development.



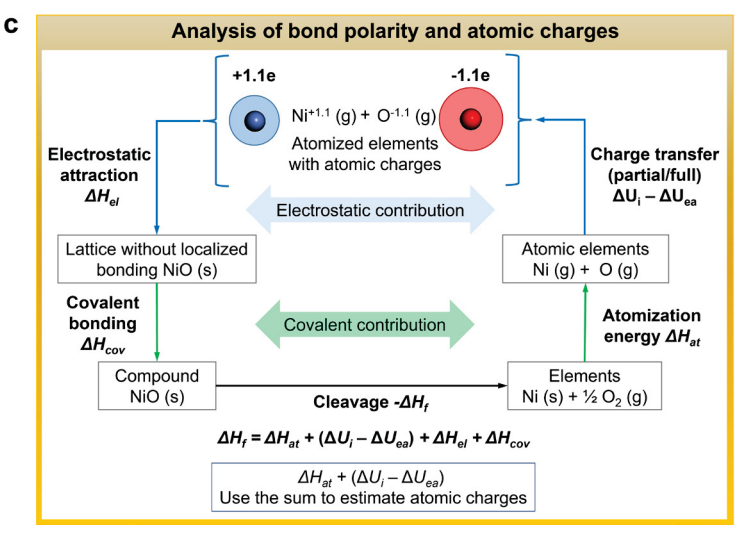


Figure 1. Overview of uses for metal oxides and hydroxides, crystal structures, and the quantitative determination of bond polarity. (a) Major applications of metal oxides and hydroxides include (clockwise from top left) structural materials such as glass and certain building materials (lime), corrosion protection, ceramics and refractories for resistance to high temperatures, catalysts for energy conversion (reproduced with permission from ref. 4), electronic devices, and medical uses (reproduced with permission from ref. 17). (b) The INTERFACE force field (IFF) was extended for the 9 oxides and hydroxides shown. The crystal structure, space group, and stoichiometry is indicated, including three 2:3 oxides of corundum structure (α-Al₂O₃, α-Cr₂O₃, α-Fe₂O₃), three 1:1 oxides of rocksalt structure (CaO, MgO, NiO), and three hydroxides (β-Ca(OH)₂, β-Mg(OH)₂, β-Ni(OH)₂). (c) Covalent and ionic contributions to chemical bonding were analyzed using a thermodynamic cycle, the extended Born model. Shown for the example of NiO, the extended Born model assists in estimating atomic charges for new compounds relative to compounds with known atomic charges, similar chemistry, and similar coordination numbers within ±10% reliability.

The oxides and hydroxides have borderline chemistries between covalent and ionic of about 50% ionic nature. We chose to derived nonbonded models without explicit terms for covalent bonding, with the exception of O-H bonds in hydroxides that tend to be less than 50% ionic (H charges <0.5 e). ^{26, 41} Accordingly, we assumed nonbonded models with respect to the metal and oxide species that incorporate remaining covalent contributions through minor increases in atomic charges and in Lennard-Jones (LJ) well depths (Figure 2a, b). The atomic charges remain close to verifiable internal dipole moments (within 10% to 20%) and follow the extended-Born model. Nonbonded models have some advantages over bonded models such as the possibility to simulate

changes in crystal structure, composition, and defect formation, as well as other forms of reactivity without added parameters. Bonded models, if chosen, would require modifications of atomic connectivity and parameters to model such processes, which is harder to implement and limits broader applicability.

The proposed models can represent structures from unit cells with few atoms to billions of atoms with excellent reproduction of crystal structures, lattice parameters, density, surface energy, bulk modulus, and interfacial properties relative to experimental data (Table 1).²⁶ The upper limit in scale are micrometers, depending on available computing resources and software for molecular simulations. For example, GROMACS⁴⁴ can be recommended for high computational efficiency. In comparison to existing popular atomistic models for oxides and hydroxides such as Pedone et. al.,⁴⁵ DFT calculations,⁴⁶⁻⁴⁸ ReaxFF,^{49, 50} ClayFF^{51, 52} and UFF,⁵³ the IFF nonbonded models show order-of-magnitude improved accuracy and compatibility, enabling far more accurate simulations and new fields of application (Table 1).

The average deviation in the computed mass density from experiment with the IFF models is only 0.2% compared to a range from 2.5% to a massive 111% deviation in earlier models. A comparison of IFF lattice parameters with DFT lattice parameters from the AFLOW database and with interatomic potentials reported in the Open Knowledgebase of Interatomic Models (OpenKIM)^{54, 55} provides further details (Table S1 and Sections S1 an S2 in the Supporting Information).⁴⁶

The computed surface energy of the IFF models is the key predictor for the performance in simulations of electrolyte and biomolecular interfaces²⁶ and deviates on average 8% from experiment, facilitating reliable simulations of interfaces and adsorption. In contrast, earlier force fields incur large errors between 45% and 75% (~25% in DFT) which make meaningful

simulations of hybrid materials difficult or impossible (Table 1). The surface energy could not be computed with the Pedone potential (Section S3 in the Supporting Information).

The average deviation of computed bulk moduli from experimental measurements is 6% using the IFF models, which compares to a range from 5% deviation with the Pedone models to very large deviations of 445% using UFF (Table 1). UFF does not achieve trustworthy predictions and is thus not recommended.

Compatibility and transferability of the parameters are important for broader utility. IFF can be used with validated water models (e.g. flexible SPC, TIP3P), 30, 35, 56, 57 biomolecular force fields (CHARMM, GROMOS, AMBER), as well as force fields for organic molecules (OLPS-AA, PCFF, CFF, COMPASS, DREIDING) with minimal loss in accuracy, featuring the best compatibility and transferability among available models. 34, 58, 59 The Pedone potential and ReaxFF are only self-compatible and cannot take advantage of the large chemical space of multicomponent electrolytes and biomolecules (proteins, DNA, lipids, carbohydrates) offered by other force fields. Specifically, the Pedone models cannot be applied to aqueous and organic interfaces. ClayFF can be used with water models and biomolecular force fields in principle (Table 1). However, intrinsic errors in the representation of chemical bonding 42, 60 and in the physical justification of the LJ parameters, along with specific cutoff settings, amplify the uncertainties in ClayFF in combination with other force fields, which have some inconsistencies of their own.

With regard to interpretability, IFF, ClayFF, and UFF include atomic charges and LJ parameters that are related to chemical bonding, atomic size, and atomic polarizability (Table 1). Left emphasizes a physical interpretation of all parameters in depth, while ClayFF and UFF do not. ClayFF uses inconsistent atomic charges, e.g., Si being more ionic than Al, and LJ parameters have a limited rationale, such as ε values near zero for metal ions and excessively large ε values

for oxygen.^{51, 52} UFF parameters have no documented rationale and validation for oxide materials, resulting in almost random computed properties (Table 1).⁵³ Simulations with UFF, arguably, create more problems and confusions than they could solve. The Pedone potential⁴⁵ and ReaxFF^{49, 50, 61-64} entail a large number of empirical terms that can be difficult to understand and modify even for expert users. For example, ReaxFF comprises ca. 30 interconnected parameters for bond order correction terms for each oxide.

The runtime (wall time) of simulations with the various force fields is similar. ReaxFF is ~50 times slower than IFF (Table 1). In terms of chemistry coverage, IFF, ReaxFF, and UFF can represent all 9 oxides and hydroxides discussed here. ReaxFF uses only one force field type for each element and requires different parameter sets to cover specific oxides and hydroxides. As a result, the simulation of mixed oxides and combinations of oxides and hydroxides in the same simulation is limited as the parameters may not fit into a single parameter set.

In an overall quality comparison, simulations with IFF are several times more reliable than with ClayFF and Pedone models (Table 1). CLAYFF has an average error of 8% in density, and surface energies with 45% average deviation are rather uncertain. The modulus with 24% average deviation is qualitatively justified. Also, ClayFF does not cover all compounds validated here. The Pedone models reproduce lattice parameters and bulk moduli in high quality, however, surface and interface properties are not accessible, and the rationale for the parameters is inconsistent (e.g., many different metal ions have the same atomic charge and other parameters are empirically fitted to elastic constants, not energy differences). The performance of ReaxFF is lower than ClayFF and borders on that of UFF, including high average deviations of 11% in density, 75% in surface energy, and 44% in bulk modulus. Uncertainties of this magnitude for critical properties of potential reactants (oxides) and products (hydroxides) raise concerns to what extent the

implementation of reactivity adds value. Also, a uniform ReaxFF parameter set may be a challenge due to the limitation to one atom type for oxygen (and for every element in general).

In addition to force fields, ab-initio calculations of Hartree-Fock type and plane-wave DFT have been widely used to compute properties of oxides, hydroxides, and organic interfaces at the small nanoscale. The major benefit of DFT and equivalent methods consists in adding the electronic structure and associated optical, spectroscopic, reactive, and conduction properties. The reliability of lattice parameters, surface energies, and adsorption properties is dependent on the density functional, types of dispersion correction, and other options, with approximately 100 choices available (e.g. PBE-D3, HSE, MN15, M06, rPBE, TPSSh).65,66 The outcomes are often uncertain with errors in lattice parameters of several percent, up to 50% in surface energies (~25%) common), and up to 30% in bulk moduli (~15% common) (Table 1). Computed binding energies of molecules to oxide surfaces are often unreliable, e.g., NO adsorption on Ni (100) shows between 30% and 100% error relative to experimental data, CO adsorption up to 300%. 65, 66 In case of handpicked density functionals with multiple empirical corrections, deviations can be reduced to ~20% for specific molecule-surface combinations. IFF, in comparison, is ~10 times more accurate in lattice parameters (~0.2% error), 2 to 5 times more accurate in surface energies (<10% error), about twice as accurate in bulk moduli (~6% error), and 2 to 10 times more accurate in adsorption energies of organic molecules (~10% error). Overall, IFF enables nearly an order of magnitude in improvement and contains no hidden parameters or correction functions. Another major difference is that DFT, or more reliable high-level QM methods (MP2, CCSD(T)), are limited to thousands or hundreds of atoms and require enormous computational power, about one to ten million times more than IFF for the same system size. DFT and CCSD(T) calculations often assume hypothetical temperatures of 0 K, in contrast to standard temperature and pressure. Equilibrium solid-electrolyte

interfaces at 0 K, for example, would then freeze to ice and expand ~10% in volume, which is not useful for practical applications.⁶⁷ Dynamic properties of oxides, oxide-electrolyte, and oxide-polymer interfaces cannot be evaluated or are severely restricted in length and time scales.

In summary, we introduce a set of IFF parameters for oxides and hydroxides that reaches one to two orders of magnitude improvement over earlier force fields and enables accurate simulations of bulk and interfacial properties due to conceptual clarity, interpretability of the parameters, and in-depth validation of key properties. IFF also outperforms the reliability of current density functionals by 2 to 10 times at a millionth fraction of the computational cost. In the following, we discuss the IFF functional forms, protocols for parameter derivation, and force field parameters. Then, results for the computed density, lattice parameters, surface energy and bulk modulus are described in comparison to available experimental data. We illustrate four applications of the IFF models, including the simulation of mixed oxides, cation migration energies, binding energy of water and organic molecules, as well as modifications of oxide surface models in aqueous solutions for different pH values. The manuscript ends with conclusions and a section on computational methods to share details of model building, visualization, calculations of the crystal structure, surface energy, bulk modulus, cation migration, molecular binding energies, sensitivity of model parameters, uncertainties and limitations. The Supporting Information includes further details, simulation-ready molecular models and force field files, and run scripts to reproduce the data.

Table 1. Summary of characteristics of the IFF models for the 9 oxides and hydroxides relative to earlier models, including Pedone et al,⁴⁵ typical density functionals (PBE, LDA, dispersion corrected), ReaxFF,⁶¹⁻⁶⁴ ClayFF,^{51,52} and UFF⁵³. For IFF, 4 options are given which correspond to IFF parameters customized for energy expressions using different Lennard-Jones functions (12-6,

9-6) and 12-6 combination rules for $r_{min,ij}$ (geometric, arithmetic). These groups include IFF-CVFF, OLPS (12-6, geometric); IFF-CHARMM, AMBER (12-6, arithmetic); IFF-PCFF (9-6); and IFF-PCFF-HQ (using higher charges for a best fit with the 9-6 LJ potential).

Property	IFF (CVFF/OPLS, CHARM/AMBER, PCFF, PCFF-HQ)	Pedone	DFT	ClayFF	ReaxFF	UFF
Reference	This work	ref. 45	refs. 46-48	refs. 51, 52	refs. 61-64	ref. 53
Avg deviation in density	0.1 %, 0.2%, 0.2%, 0.2%,	2.5 %	~4 %	8 %	11 %	111 %
Avg deviation in surface energy from expt	5%, 8%, 7%, 8%	Could not be	~25 %	45 %	75 %	71 %
Avg deviation in bulk modulus from expt	4 %, 5%, 21%, 7%	5 %	~15 %	24 %	44 %	445 %
Compatibility for aqueous interfaces	Yes	No	Yes	Yes	No	Yes
Compatibility with FFs for biomolecules (CHARMM, AMBER, GROMOS)	Yes	No	NA	Yes	No	Yes
Compatibility with FFs for organic molecules (OPLS-AA, PCFF, CFF, COMPASS, DREIDING)	Yes	No	NA	Yes	No	No

Interpretability (High/Medium/Low)	High	Medium (inconsist. rationale)	Low (many terms/params.)	Medium (inconsist. rationale)	Low (many terms/params.)	Low (poor rationale)
Simulation time (1.0 = fastest)	1	1	10 ⁻⁶	1	0.02	1
Parameter availability a (9 = all 9 compounds)	9	6	9	6	9 ^b	9

2. Results and Discussion

2.1. Development of IFF Oxide and Hydroxide Parameters. IFF relies on bonded models in case of predominantly localized, covalent bonding between neighbor atoms (>50% covalent) and on nonbonded models in case of predominantly ionic bonding (<50% covalent and >50 % ionic or metallic) for compounds across the periodic table (Figure 2).²⁶ The physical representation of chemical bonds according to this rationale is essential and deviations would result in loss of accuracy and transferability. Metal oxides and hydroxides have both types of bonding. The 9 core compounds lean more towards ionic bonding (Figure 2a), and silica is predominantly covalent. Nonbonded models, if physically justified, have the advantages of a simple energy expression and

^a The score in the parameter availability category equals the number of compounds covered. Some potentials cover all 9 oxides and hydroxides considered here and some 6 oxides and hydroxides. The reported average deviations and characteristics are based on the covered compounds. ^b Simulations of mixed oxides and hydroxides may be limited with ReaxFF due to the necessity for multiple distinct parameter sets.

fewer parameters, resulting in applicability to mixed solid phases and certain chemical reactions, which is not feasible using bonded models. However, nonbonded models have a higher sensitivity to combination rules of LJ parameters than bonded models because interatomic distances are solely represented by the LJ parameters. Differences in combination rules in bonded models often still allow transferability with marginal loss in accuracy.^{30, 31, 35, 42, 60, 68}

The nonbonded oxide models use only two terms, Coulomb interactions and van der Waals interactions via a LJ potential, to describe the total potential energy (Figure 2a). OH surface groups or hydroxide ions in hydroxide minerals with predominantly covalent O-H bonds continue to use an additional harmonic bond stretching potential to describe the O-H bonds (Figure 2b). The overall energy expression then consists of bond, Coulomb and van der Waals energy terms, whereby IFF offers the options of 12-6 or 9-6 forms of the LJ potential (Figure 2c). Bonded compounds can be included with their full set of bonded potentials in the same simulation and both nonbonded and bonded models have unlimited coexistence and compatibility within IFF. The IFF parameters are given in Table 2.

The workflow to tune the models started with a crystal structure from X-ray diffraction data, preferentially the most accurate available measurements (Figure 2d). $^{10\text{-}16}$ Initial atomic charges, atom types, and LJ parameters were assigned according to their chemical environment. The atomic charges rely on experimental sources and chemical theory in IFF (Figure 1c). 41 For example, atomic charges of $+1.5\pm0.1$ e on Cr atoms and -1.0 ± 0.1 e on O atoms in escolaite, α -Cr₂O₃, were determined from X-ray deformation electron densities. 69 Atomic charges in corundum, α -Al₂O₃, are expected to be between $+1.32\pm0.05$ e and $+1.47\pm0.26$ e according to measurements for octahedral corundum, 40 diaspore, 38 and tetrahedral AlPO₄, which is isoeletronic with SiO₂. 70 Furthermore, the extended Born model and comparisons to chemically similar compounds with

known atomic charges were employed (Figure 1c), which is critical for the better performance of IFF as a whole (Table 1).⁴¹ Initial values of the LJ parameter r_{min} take into account known crystallographic radii across the periodic table.⁷¹ Hereby, the nonbonded models utilize smaller r_{min} values for the metals than equivalent bonded models.^{26, 43, 68, 72} Smaller atomic radii are required to reproduce the metal-oxygen bond lengths in the absence of bonded terms, to accommodate the absence of customary exclusions of nonbonded interactions between 1,2 and 1,3 bonded atoms, and the values correlate with a smaller cloud of valence electrons due to the increased atomic charge. Well-depths ε_0 play a dual role by contributing to both repulsion between atoms at short distance and to minor attractive dispersion interactions at distances larger than r_{min} .²⁶ Using the initial parameters, the equilibrium crystal structure, surface energies for the (hkl) cleavage plane of lowest energy, and bulk modulus were computed using molecular mechanics and molecular dynamics simulations in the NPT and NVT ensembles for validation and subsequent iteration.

Upon analysis of deviations in computed properties from experimental data, the charges q and the LJ parameters r_{min} and ε_0 were iteratively adjusted to better reproduce bulk and surface properties. Hereby, iterations mainly involved the LJ parameters and atomic charges were modified in a smaller range as necessary since the representation of chemical bonding is not a fit parameter in IFF. The validation was focused on the structure and energy differences (surface energy), not on structure and modulus (as the modulus does not enter the Hamiltonian). Higher atomic charges tend to increase the density, the surface energy, and the modulus. Larger values of r_{min} decrease the density, surface energy, and the modulus. Larger values of ε_0 also tend to decrease the density due to added repulsion in the predominantly ionic model. However, larger values of ε_0 also tend to increase the surface energy and the modulus due to a deeper potential well near

equilibrium. The final models typically reproduce the crystal structure, density, and lattice parameters within 0.5% deviation from experiments, surface energies within 5% of the target value, and bulk moduli within 5% of experimental reference data (Table 2). Bonded parameters for OH^- ions were assigned utilizing the equilibrium bond length $r_{\theta, ij}$ from X-ray data and an equilibrium bond constant k_{ij} , which was tuned to match the bond stretching band in the experimental IR spectra (Table 3). The agreement between simulation and experimental measurements is better than 1% in bond lengths and 3 cm⁻¹ in wavenumbers (Table 4). The models also reproduced the average M-O-H bond angles from X-ray data of about 120° without additional parameters with less than 2° deviation in molecular dynamics simulations. We observed significant instantaneous fluctuations of the M-O-H bond angles on the order of $\pm 15^{\circ}$ (Table 4). The parameter iterations involved several thousand molecular mechanics and molecular dynamics simulations in total.

Upon completion of validation, the models were consistent in the representation of chemical bonding, structure, and relative energies (Table 2). They are also compatible with and transferable to other force fields and can be used to compute a multitude of non-fitted bulk and interfacial properties without further adjustments. The chosen atomic charges in the nonbonded models are 10% to 20% higher than the physically justified values (which correlate with true multipole moments). Even larger increases in atomic charges were necessary in the PCFF-HQ version using the 9-6 LJ potential to enable accurate predictions of the bulk modulus (Table 2). The trend towards higher atomic charges than expected for true chemical bonding compensates for the missing covalent bonding contributions in the model and appears to be acceptable for practical applications.

The nonbonded parameters are, as mentioned earlier, sensitive to mixing rules, i.e., to the automated calculation of LJ parameters for pairs of different atom types i and j. Therefore, specific IFF parameters are given for 12-6 LJ potentials that use arithmetic combination rules for $r_{min, ij}$, as in CHARMM and AMBER, as well as for 12-6 LJ potentials that use geometric combination rules for $r_{min, ij}$ as in OPLS-AA and CVFF (for ε_{ij} , all force fields use geometric combination rules). If the specific nonbonded parameters were transferred from one of these groups to the other, we observed several percent deviations in lattice parameters, up to 15% percent deviation in surface energies, and up to 25% in bulk moduli. 9-6 LJ potentials in PCFF, COMPASS and corresponding HQ versions use Waldmann-Hagler (6th power) combination rules.

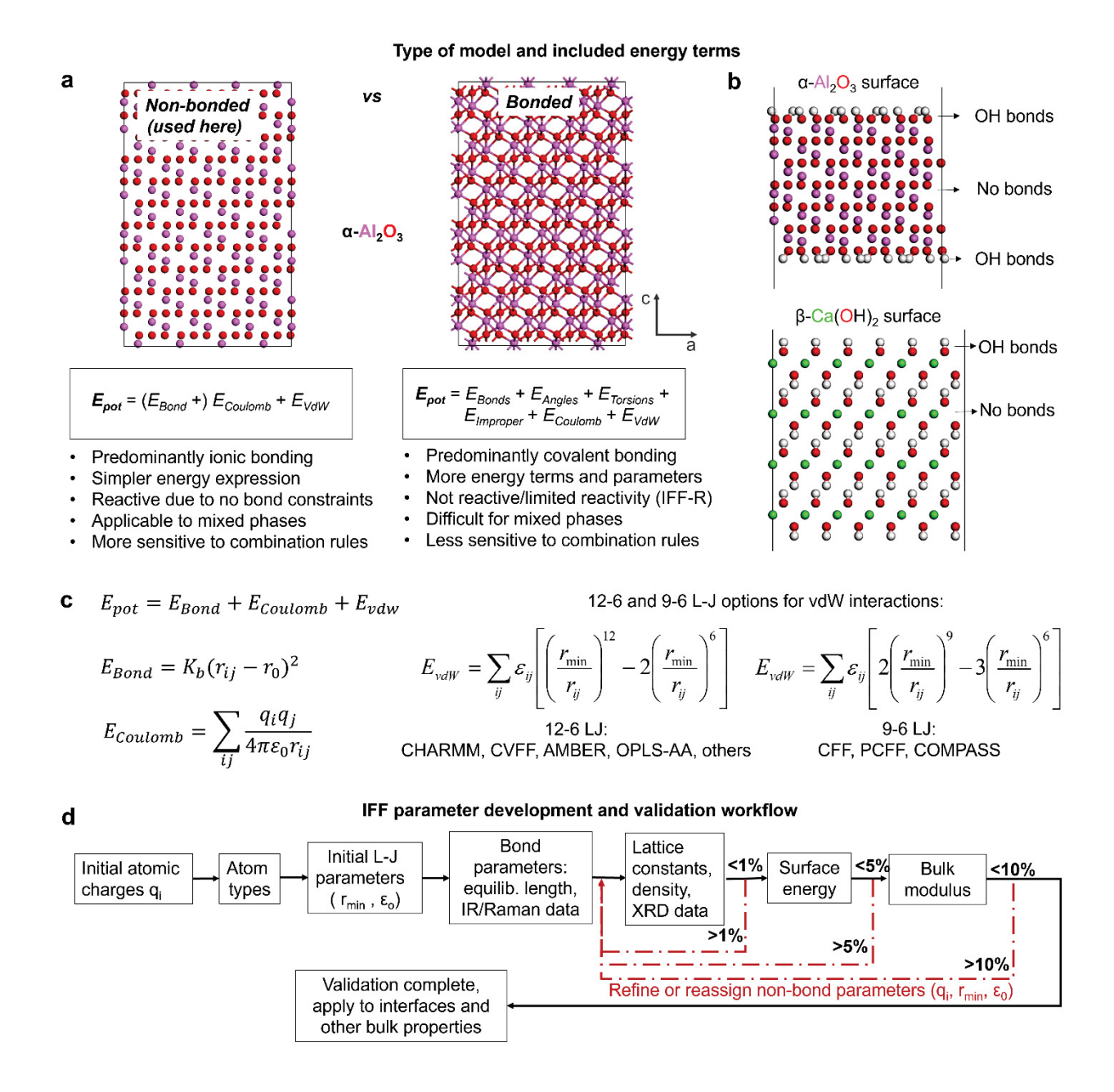


Figure 2. Nonbonded versus bonded models and the workflow for parameter development. (a) Comparison of structural representation, energy terms, and utility of nonbonded and bonded models. Nonbonded models can be applied when covalent contributions to bonding are approximately 50% or less than ionic contributions to bonding. They offer more flexibility to simulate different polymorphs and mixed chemistries in comparison to models with explicit bonded terms. (b) O-H bonds can be present on the hydroxylated surface layer of oxides in case of

aqueous conditions (example of α -Al₂O₃ shown) or in the crystal structure of hydroxides (example of β -Ca(OH)₂ shown). (c) Energy terms in the nonbonded models include the Coulomb energy and the van-der-Waals energy, either in 12-6 LJ or in 9-6 LJ form. Hydroxide models also use a harmonic energy term for the predominantly covalent O-H bond in the potential energy expression, $E_{Bond} = k_{ij}(r_0 - r_{ij})^2$. Force fields compatible with IFF, such as CHARMM or OPLS-AA, employ different combination rules for 12-6 LJ potentials, which are specifically accounted for in our nonbonded IFF models. (d) The workflow for the development of IFF parameters for oxides and hydroxides. Initially, atomic charges, atom types, and LJ parameters are assigned, using experimental data and analogies to similar validated chemistry covered in IFF. Tests of computed crystal structure, surface energy, and bulk modulus provided feedback for refinements to minimize deviations.

Table 2. IFF nonbonded parameters for the oxides and hydroxides. OPLS, CVFF, CHARMM, and AMBER utilize a 12-6 Lennard-Jones potential. PCFF and PCFF-HQ use a 9-6 Lennard-Jones potential. IFF-OPLS, CVFF use a geometric mixing rule for rmin, ij whereas IFF-CHARMM, AMBER use an arithmetic mixing rule.

Compound	IFF option	Ato	Atomic charges	rges		Lennard-J	Lennard-Jones parameters	S
		q _M (e) ^a	do (e)	фн (е)	rmin, M (Å)	rmin, O (Å)	rmin, o (Å) EM (kcal/mol)	E0 (kcal/mol)
α-ΑΙ2Ο3	IFF-OPLS, CVFF	1.62	-1.08	NA	1.72	3.3	0.45	0.35
	IFF-CHARMM, AMBER	1.62	-1.08	NA	1.86	3.54	0.1	0.09
	IFF-PCFF	1.62	-1.08	NA	1.81	3.45	0.35	0.2
	IFF-PCFF-HQ	1.77	-1.18	NA	2.2	3.77	0.08	0.1
α-Cr ₂ O ₃	IFF-OPLS, CVFF	1.65	-1:1	NA	1.96	3.43	0.35	0.25
	IFF-CHARMM, AMBER	1.65	-1.1	NA	1.93	3.44	0.2	0.2
	IFF-PCFF	1.65	-1.1	NA	1.85	3.41	0.45	0.4

	IFF-PCFF-HQ	1.86	-1.24	NA	2.28	3.81	0.11	0.14
α-Fe ₂ O ₃	IFF-OPLS, CVFF	1.74	-1.16	NA	2.08	3.51	0.3	0.2
	IFF-CHARMM, AMBER	1.74	-1.16	NA	2.03	3.48	0.2	0.2
	IFF-PCFF	1.74	-1.16	NA	1.98	3.43	0.45	0.42
	IFF-PCFF-HQ	1.92	-1.28	NA	2.26	3.73	0.17	0.2
MgO	IFF-OPLS, CVFF	1.06	-1.06	NA	2.06	3.35	0.4	0.3
	IFF-CHARMM, AMBER	1.06	-1.06	NA	1.90	3.35	0.4	0.3
	IFF-PCFF	1.06	-1.06	NA	2.04	3.32	0.4	0.4
	IFF-PCFF-HQ	1.22	-1.22	NA	2.46	3.56	0.2	0.15
CaO	IFF-OPLS, CVFF	1.23	-1.23	NA	2.94	3.33	0.3	0.25
	IFF-CHARMM, AMBER	1.23	-1.23	NA	2.90	3.35	0.3	0.25
	IFF-PCFF	1.23	-1.23	NA	3.33	3.49	0.35	0.15

	IFF-PCFF-HQ	1.36	-1.36	NA	3.47	3.77	0.2	0.1
NiO	IFF-OPLS, CVFF	1.10	-1.1	NA	1.95	3.4	0.35	0.4
	IFF-CHARMM, AMBER	1.10	-1.1	NA	1.87	3.32	0.35	0.4
	IFF-PCFF	1.10	-1.1	NA	2.02	3.3	0.42	0.42
	IFF-PCFF-HQ	1.35	-1.35	NA	2.54	3.83	0.1	0.1
β-Mg(OH) ₂ ^b	IFF-OPLS, CVFF	1.40	-1.10	0.40	2.19	3.59	0.25	0.2
	IFF-CHARMM, AMBER	1.35	-1.02	0.345	1.94	3.51	0.3	0.25
	IFF-PCFF	1.40	-1.10	0.40	2.14	3.71	0.25	0.2
	IFF-PCFF-HQ	1.50	-1.20	0.45	2.27	3.88	0.15	0.15
β-Ca(OH)2 ^b	IFF-OPLS, CVFF	1.70	-1.32	0.47	3.00	3.48	0.2	0.4
	IFF-CHARMM, AMBER	1.70	-1.32	0.47	2.96	3.59	0.2	0.25
	IFF-PCFF	1.70	-1.32	0.47	3.30	3.85	0.25	0.15

IFF-PCFF-HQ	łQ	1.70	-1.40	-1.40 0.55 3.32	3.32	3.91	0.25	0.15
IFF-OPLS, CVF	CVF	1.41	-1.02	0.315 2.15	2.15	3.53	0.25	0.2
FF-CHARI	IFF-CHARMM, AMBER	1.36	-0.96	0.28	1.94	3.44	0.30	0.25
IFF-PCFF		1.41	-1.02	0.315 2.17	2.17	3.60	0.25	0.2
IFF-PCFF-HQ	łQ	1.51	-1.12	0.365	2.45	3.89	0.1	0.1

of covalent bonding contributions. In addition, while ionic bonding is stronger in Al₂O₃ than in Cr₂O₃ and in Fe₂O₃, the atomic charges +1.00e, 1.15e, and +0.95e; as well as for Mg, Ca, and Ni in the hydroxides +1.3e, +1.55e, and +1.2e with an uncertainty of $\pm 5\%$ to ^a The atomic charges in the nonbonded model reflect contributions by ionic bonding and by additional covalent bonding. The atomic charges for the metal atoms in the nonbonded models are therefore higher (and upper limits) for true atomic charges due to the neglect and Fe oxides can only be represented by added Coulomb interactions in this simplified model due to the absence (and less practical implementation) of additional covalent bonded terms. For the same reason, the charge on Ni is higher than Mg in the oxide and hydroxide. Physical charge assignments for Al, Cr, and Fe in the oxides are +1.4e, +1.35e, and +1.30e; for Mg, Ca, Ni in the oxides for Cr and Fe are larger than that for Al in the nonbonded models. Hereby, additional d electrons and stronger covalent bonding in Cr

following earlier IFF and water models. The atomic charges on the H atoms correlate with chemical bonding and solubility products of the hydroxides. Using 12-6 LJ parameters, the LJ contribution is effectively zero using $r_{min} = 0.0001 \text{ Å}$ and $\epsilon = 0.0001 \text{ kcal/mol}$. Using 9-6 LJ parameters (PCFF and PCFF-HQ), the contribution is $r_{min} = 1.085 \text{ Å}$ and $\epsilon = 0.015 \text{ kcal/mol}$. These values could also be set to ^b Hydrogen atoms in hydroxide ions are represented mainly by atomic charges and with essentially negligible Lennard-Jones parameters, effectively zero without loss (since $r_{min} = 1.085 \text{ Å}$ and $\epsilon = 0.015 \text{ kcal/mol}$ is already very small).

Table 3. IFF bonded parameters in O-H groups of the metal hydroxides.

Hydroxide	$\mathbf{r}_0\left(\mathrm{\AA} \right)$	$k_0 (kcal/mol/{^2})$
$\beta ext{-Mg(OH)}_2$	0.95	530
β-Ca(OH) ₂	0.91	520
β -Ni(OH) $_2$	1.10	515

Table 4. Comparison of average O-H bond lengths, O-H bond stretch vibrations, and M-O-H bond angles in the hydroxides according to X-ray data and IR spectra with values obtained in molecular dynamics simulations with IFF at 298 K. The M-O-H bond angles exhibit significant temporary fluctuation, which are shown as a standard deviation. The results are independent of the IFF energy expressions with the given error bars.

	O-H bond len	d length (Å)	IR vibration, O-H	IR vibration, O-H bond stretch (cm ⁻¹)	M-O-H b	M-O-H bond angle (°)
Hydroxide	Experiment	MD simulation	Experiment	MD simulation	Experiment	MD simulation
β-Mg(OH) ₂	0.970ª	0.980	3652 ^d	3648	119.8ª	121±14
β -Ca(OH) ₂	0.907 ^b	0.917	3617°	3616	118.9 ^b	120±11
β -Ni(OH) $_2$	1.128°	1.129	3581^{f}	3583	122.5°	120±16

^aRef. ¹⁶. ^bRef. ¹³. ^cRef. ¹⁰. ^dRef. ⁷³. ^eRef. ⁷⁴. ^fRef. ⁷³.

2.2. Crystal Structure. The reference data for crystal structures and lattice parameters were chosen from X-ray and neutron diffraction as reported in the American Mineralogist Crystal Structure Database (AMCSD) (Table 5). The measurement uncertainties in lattice parameters are on the order of 0.1%, and sometimes higher as indicated in Table 5. The IFF parameters of oxides and hydroxides were tuned to reproduce these lattice parameters in molecular dynamics simulations at 298 K and 1 atm using the NPT ensemble, i.e., constant number of particles, pressure, and temperature (Table 5). The average deviations in density and lattice parameters using IFF are ±0.2% and <±0.2%, respectively, with maximum deviations of ±0.7% and ±0.75%, respectively, compared to the XRD data (Table 1). Cell angles always agree within ±0.05% (Table 5). The computed results for the Pedone potential, ReaxFF, ClayFF and UFF are included for comparison. Average errors with these methods range from few % to larger than 100%, whereby individual differences start at 0.3% (ClayFF for MgO) to extreme errors of 43270% (UFF for Ca(OH)₂). Earlier methods are, on balance, one to three orders of magnitude less accurate than IFF and inconsistent across different chemistry. IFF stays close to experimental accuracy.

Benchmarking with DFT results in the AFLOW database,⁷⁶ reactive, and other nonbonded potentials is possible using the OpenKIM project,^{54, 55} which has been recently extended to include bonded potentials (Table S1 and Sections S1 and S2 in the Supporting Information). Average deviations using DFT calculations are approximately 10x larger compared to IFF, specifically, ~4% in density and ~2% in lattice parameters (refs. ⁴⁶⁻⁴⁸ and Table S1 in the Supporting Information). OpenKIM comparisons are currently limited to lattice parameters.

Table 5. Comparison of density and lattice parameters according to experimental data from X-ray diffraction, calculated in this work using 12-6 LJ (IFF-CVFF, OLPS and IFF-CHARMM, AMBER) and 9-6 LJ parameters (IFF-PCFF and IFF-PCFF-HQ), and other popular atomistic simulation techniques (Pedone et. al., ReaxFF, ClayFF and UFF). The uncertainty in experimental data is indicated using multiple crystal structures reported under standard conditions in the AMCSD. Deviations of the computed lattice parameters relative to experimental data are indicated.

Source	Density (g/cm ³)	a (Å)	b (Å)	c (Å)	α (°)	β (°)	γ (°)
α-Al ₂ O ₃		(4x4x2 Superce	ell)			
Experiment ^{a,b}	3.987	19.036	19.036	25.982	90	90	120
Uncertainty	±0.003	±0.011	±0.011	±0.005	0	0	0
IFF-CVFF, OPLS	3.997	18.956	18.956	26.139	90	90	120
Dev from expt	0.3%	-0.4%	-0.4%	0.6%	0%	0%	0%
IFF-CHARMM, AMBER ^c	3.986	19.039	19.039	25.979	90	90	120
Dev from expt	0.0%	0.0%	0.0%	0.0%	0%	0%	0%
IFF-PCFF	3.981	19.095	19.095	25.863	90	90	120
Dev from expt	-0.2%	0.3%	0.3%	-0.5%	0%	0%	0%
IFF-PCFF-HQ	3.984	19.071	19.071	25.907	90	90	120
Dev from expt	-0.1%	0.2%	0.2%	-0.3%	0%	0%	0%
Pedone et.al.d	4.062	18.845	18.845	26.024	90	90	120

Dev from expt	1.9%	-1.0%	-1.0%	0.1%	0%	0%	0%
ReaxFF-1e	3.477	20.027	19.772	27.260	90	90	120
Dev from expt	-13%	5.2%	3.9%	4.9%	0%	0%	0%
ReaxFF-2 ^f	3.950 ^a		Not provid	led in original	paper		
Dev from expt	-0.9%		Not provid	led in original	paper		
ClayFF ^{c,g}	3.676	19.492	19.492	26.847	90	90	120
Dev from expt	-7.8%	2.4%	2.4%	3.3%	0%	0%	0%
$\mathrm{UFF^{h}}$	6.354	16.308	16.308	22.214	90	90	120
Dev from expt	64%	-14.3%	-14.3%	-14.5%	0%	0%	0%
α-Cr ₂ O ₃		(4x4x2	Supercell)				
Experiment ^{a,b}	5.225	19.843	19.843	27.198	90	90	120
Experiment ^{a,b} Uncertainty	5.225 ±0.014	19.843 ±0.016	19.843 ±0.016	27.198 ±0.026	90 0	90 0	120 0
•							
Uncertainty	±0.014	±0.016	±0.016	±0.026	0	0	0
Uncertainty IFF-CVFF, OPLS	±0.014 5.215	±0.016 19.888	±0.016 19.888	±0.026 27.127	0 90	0 90	0 120
Uncertainty IFF-CVFF, OPLS Dev from expt IFF-CHARMM,	±0.014 5.215 -0.2%	±0.016 19.888 0.2%	±0.016 19.888 0.2%	±0.026 27.127 -0.3%	0 90 0%	0 90 0%	0 120 0%
Uncertainty IFF-CVFF, OPLS Dev from expt IFF-CHARMM, AMBER ^c	±0.014 5.215 -0.2% 5.208	±0.016 19.888 0.2% 19.843	±0.016 19.888 0.2% 19.842	±0.026 27.127 -0.3% 27.198	0 90 0% 90	0 90 0% 90	0 120 0% 120
Uncertainty IFF-CVFF, OPLS Dev from expt IFF-CHARMM, AMBER ^c Dev from expt	±0.014 5.215 -0.2% 5.208	±0.016 19.888 0.2% 19.843 0.0%	±0.016 19.888 0.2% 19.842 0.0%	±0.026 27.127 -0.3% 27.198	0 90 0% 90	0 90 0% 90	0 120 0% 120
Uncertainty IFF-CVFF, OPLS Dev from expt IFF-CHARMM, AMBER ^c Dev from expt IFF-PCFF	±0.014 5.215 -0.2% 5.208 -0.3% 5.193	±0.016 19.888 0.2% 19.843 0.0% 19.961	±0.016 19.888 0.2% 19.842 0.0% 19.961	±0.026 27.127 -0.3% 27.198 0.0% 27.047	0 90 0% 90 0% 90	0 90 0% 90 0%	0 120 0% 120 0% 120

Pedone et.al.d	5.141	20.007	20.007	27.189	90	90	120
Dev from expt	-1.6%	0.8%	0.8%	0.0%	0%	0%	0%
ReaxFF ^e	4.807	21.107	21.107	26.127	90	90	120
Dev from expt	-8.0%	6.5%	6.5%	-3.9%	0%	0%	0%
ClayFF ^{c,g}		Pa	arameters for C	r ₂ O ₃ not availal	ble		
UFF^{h}	6.489	18.840	18.840	24.472	90	90	120
Dev from expt	24%	-4.9%	-4.9%	-10.0%	0%	0%	0%
α-Fe ₂ O ₃			(4x4x2 Super	cell)			
Experiment ^{a,b}	5.246	20.152	20.152	27.544	90	90	120
Uncertainty	±0.016	± 0.007	± 0.007	± 0.029	0	0	0
IFF-CVFF, OPLS	5.247	20.211	20.211	27.427	90	90	120
Dev from expt	0.0%	0.3%	0.3%	-0.4%	0%	0%	0%
IFF-CHARMM, AMBER ^c	5.235	20.250	20.250	27.388	90	90	120
Dev from expt	-0.2%	0.5%	0.5%	-0.6%	0%	0%	0%
IFF-PCFF	5.239	20.258	20.258	27.347	90	90	120
Dev from expt	-0.1%	0.5%	0.5%	-0.7%	0%	0%	0%
IFF-PCFF-HQ	5.259	20.217	20.217	27.351	90	90	120
Dev from expt	0.2%	0.3%	0.3%	-0.7%	0%	0%	0%
Pedone et.al.d	5.580	19.810	19.810	26.847	90	90	120
Dev from expt	6.4%	-1.7%	-1.7%	-2.5%	0%	0%	0%

ReaxFF ^e	6.145	20.002	20.003	23.911	90	90	120
Dev from expt	17%	-0.7%	-0.7%	-13.2%	0%	0%	0%
ClayFF ^{c,g}	3.966	22.358	22.358	29.653	90	90	120
Dev from expt	-24%	10.9%	10.9%	7.7%	0%	0%	0%
UFF ^h	27.917	11.559	11.555	15.767	90	90	120
Dev from expt	432%	-42.6%	-42.7%	-42.8%	0%	0%	0%
MgO		(5x5x5	5 Supercell)				
Experiment ^{a,b}	3.585	21.055	21.055	21.055	90	90	90
Uncertainty	±0.005	±0.010	±0.010	±0.010	0	0	0
IFF-CVFF, OPLS	3.582	21.061	21.061	21.061	90	90	90
Dev from expt	-0.1%	0.0%	0.0%	0.0%	0%	0%	0%
IFF-CHARMM, AMBER ^c	3.586	21.054	21.054	21.054	90	90	90
Dev from expt	0.0%	0.0%	0.0%	0.0%	0%	0%	0%
IFF-PCFF	3.577	21.071	21.071	21.071	90	90	90
Dev from expt	-0.2%	0.1%	0.1%	0.1%	0%	0%	0%
IFF-PCFF-HQ	3.582	21.061	21.061	21.061	90	90	90
Dev from expt	-0.1%	0.0%	0.0%	0.0%	0%	0%	0%
Pedone et.al.d	3.513	21.197	21.197	21.197	90	90	90
Dev from expt	-2.0%	0.7%	0.7%	0.7%	0%	0%	0%

ReaxFFe	3.466	21.294	21.294	21.295	90	90	90		
Dev from expt	-3.3%	1.1%	1.1%	1.1%	0%	0%	0%		
ClayFF ^{c,g}	3.557	21.109	21.109	21.110	90	90	90		
Dev from expt	-0.8%	0.3%	0.3%	0.3%	0%	0%	0%		
UFF ^h	1.935	25.898	25.873	25.812	90	90	90		
Dev from expt	-46%	23%	23%	23%	0%	0%	0%		
CaO (4x4x4 Supercell)									
Experiment ^{a,b}	3.337	19.260	19.260	19.260	90	90	90		
Uncertainty	±0.004	± 0.009	± 0.009	±0.009	0	0	0		
IFF-CVFF, OPLS	3.336	19.261	19.261	19.261	90	90	90		
Dev from expt	0.0%	0.0%	0.0%	0.0%	0%	0%	0%		
IFF-CHARMM, AMBER ^c	3.347	19.240	19.240	19.240	90	90	90		
Dev from expt	0.3%	-0.1%	-0.1%	-0.1%	0%	0%	0%		
IFF-PCFF	3.326	19.282	19.282	19.282	90	90	90		
Dev from expt	-0.3%	0.1%	0.1%	0.1%	0%	0%	0%		
IFF-PCFF-HQ	3.348	19.242	19.242	19.242	90	90	90		
Dev from expt	0.3%	-0.1%	-0.1%	-0.1%	0%	0%	0%		
Pedone et.al.d	3.422	19.099	19.099	19.099	90	90	90		
Dev from expt	2.5%	-0.8%	-0.8%	-0.8%	0%	0%	0%		
ReaxFFe	2.826	18.845	23.753	18.845	90	90	90		
Dev from expt	-15%	-2.3%	23%	-2.3%	0%	0%	0%		

ClayFF ^{c,g}	3.591	18.795	18.792	18.793	90	90	90	
Dev from expt	7.6%	-2.4%	-2.4%	-2.4%	0%	0%	0%	
UFF ^h	2.437	21.274	21.369	21.377	90	90	90	
Dev from expt	-27%	11%	11%	11%	0%	0%	0%	
NiO	(5x5x5 Supercell)							
Experiment ^{a,b}	6.851	20.842	20.842	20.842	90	90	90	
Uncertainty	±0.027	±0.028	± 0.028	± 0.028	0	0	0	
IFF-CVFF, OPLS	6.837	20.857	20.857	20.857	90	90	90	
Dev from expt	-0.2%	0.1%	0.1%	0.1%	0%	0%	0%	
IFF-CHARMM, AMBER ^c	6.843	20.851	20.851	20.851	90	90	90	
Dev from expt	-0.1%	0.0%	0.0%	0.0%	0%	0%	0%	
IFF-PCFF	6.843	20.851	20.851	20.851	90	90	90	
Dev from expt	-0.1%	0.0%	0.0%	0.0%	0%	0%	0%	
IFF-PCFF-HQ	6.869	20.824	20.824	20.824	90	90	90	
Dev from expt	0.3%	-0.1%	-0.1%	-0.1%	0%	0%	0%	
Pedone et.al.d	6.751	20.945	20.945	20.945	90	90	90	
Dev from expt	-1.5%	0.5%	0.5%	0.5%	0%	0%	0%	
ReaxFF ^e	5.426	22.883	22.667	22.031	90	90	90	
Dev from expt	-21%	9.8%	8.8%	5.7%	0%	0%	0%	
ClayFF ^{c,g}	Parameters not available for NiO							
UFF ^h	13.424	16.693	16.772	16.504	90	90	90	

Dev from expt	96%	-20%	-19.5%	-21%	0%	0%	0%	
β-Mg(OH) ₂	(7x7x5 Supercell)							
Experiment ^{a,b}	2.366	22.033	22.033	23.850	90	90	120	
Uncertainty	±0.003	±0.011	±0.011	±0.011	0	0	0	
IFF-CVFF, OPLS	2.366	22.054	22.054	23.818	90	90	120	
Dev from expt	0.0%	0.1%	-0.1%	-0.1%	0%	0%	0%	
IFF-CHARMM, AMBER ^c	2.363	22.011	22.018	23.919	90	90	120	
Dev from expt	-0.1%	-0.1%	-0.1%	0.3%	0%	0%	0%	
IFF-PCFF	2.359	22.100	22.108	23.770	90	90	120	
Dev from expt	-0.3%	0.3%	0.3%	-0.3%	0%	0%	0%	
IFF-PCFF-HQ	2.370	22.025	22.029	23.824	90	90	120	
Dev from expt	0.2%	0.0%	0.0%	-0.1%	0%	0%	0%	
Pedone et.al.d	Parameters not available for Mg(OH) ₂							
ReaxFF ^e	2.451	21.872	21.875	23.362	90	90	120	
Dev from expt	3.6%	-0.7%	-0.7%	-2.0%	0%	0%	0%	
ClayFF ^{c,g}	2.249	22.801	22.880	23.429	90	90	120	
Dev from expt	-4.9%	3.5%	3.5%	-1.8%	0%	0%	0%	
UFF ^h	1.247	26.186	26.191	32.028	90	96	120	
Dev from expt	-47%	19%	19%	34%	0%	0%	0%	
		.						

34

(6x6x4 Supercell)

β-Ca(OH)₂

Experiment ^{a,b}	2.244	21.555	21.555	19.620	90	90	120	
Uncertainty	±0.010	±0.021	±0.021	±0.049	0	0	0	
IFF-CVFF, OPLS	2.245	21.608	21.597	19.530	90	90	120	
Dev from expt	0.0%	0.2%	0.2%	-0.5%	0%	0%	0%	
IFF-CHARMM, AMBER°	2.243	21.535	21.533	19.670	90	90	120	
Dev from expt	0.0%	-0.1%	-0.1%	0.3%	0%	0%	0%	
IFF-PCFF	2.245	21.519	21.505	19.693	90	90	120	
Dev from expt	0.0%	-0.2%	-0.2%	0.4%	0%	0%	0%	
IFF-PCFF-HQ	2.249	21.548	21.555	19.592	90	90	120	
Dev from expt	0.2%	0.0%	0.0%	-0.1%	0%	0%	0%	
Pedone et.al.d	Parameters not available for Ca(OH) ₂							
ReaxFF ^e	2.180	21.299	21.797	24.701	90	90	120	
Dev from expt	-2.9%	1.2%	1.2%	0.6%	0%	0%	0%	
ClayFF ^{c,g}	2.263	21.720	22.181	18.756	90	90	120	
Dev from expt	0.8%	0.8%	2.9%	-4.4%	0%	0%	0%	
UFF ^h	0.126	24.105	23.990	10650	147	77	120	
Dev from expt	-94%	12%	11%	43270%	63%	-16%	0%	
β-Ni(OH) ₂	(7x7x5 Supercell)							
Experiment ^{a,b}	3.982	21.819	21.819	22.975	90	90	120	
Uncertainty	±0.017	±0.015	±0.015	± 0.078	0	0	0	

IFF-CVFF, OPLS	3.970	21.813	21.813	23.089	90	90	120
Dev from expt	-0.3%	0.0%	0.0%	0.5%	0%	0%	0%
IFF-CHARMM, AMBER ^c	3.990	21.835	21.835	22.896	90	90	120
Dev from expt	0.2%	0.1%	0.1%	-0.3%	0%	0%	0%
IFF-PCFF	3.973	21.838	21.843	22.986	90	90	120
Dev from expt	0.2%	0.1%	0.1%	0.0%	0%	0%	0%
IFF-PCFF-HQ	3.999	21.766	21.762	22.995	90	90	120
Dev from expt	0.4%	-0.2%	-0.3%	0.1%	0%	0%	0%
Pedone et.al.d	Parameters not available for Ni(OH)2						
ReaxFF ^e	5.161	15.698	15.503	25.477	90	90	120
Dev from expt	30%	-16%	-17%	11%	0%	0%	0%
ClayFF ^{c,g}	Parameters not available for Ni(OH)2						
UFF ^h	0.143	16.641	16.286	51180	81	155	121
Dev from expt	-96%	-11%	-13%	222600%	-10%	72%	1%

^{a, b} Lattice parameters were obtained using crystal structure data from X-ray diffraction, refs. ¹⁰⁻¹⁶, as catalogued in the AMCSD, ref. ⁷⁵. In case of multiple references for the same minerals, references under standard conditions were chosen to compute the standard deviation in the experimental data: α-Al₂O₃, refs. ^{18, 21-23}, α-Cr₂O₃, refs. ^{12, 18, 24-26}, α-Fe₂O₃, refs. ^{19, 25, 27}, CaO, refs. ^{10, 77}, MgO, refs. ¹¹, NiO, refs. ^{10, 78, 79}, β-Ca(OH)₂, refs. ^{10, 80-82}, β-Mg(OH)₂, refs. ^{16, 83}, and β-Ni(OH)₂, refs. ^{10, 78}.

^c Lattice parameters of IFF-CHARMM/AMBER and ClayFF were computed using larger orthogonal simulation cells and converted to the corresponding hexagonal cells for a consistent comparison. ^dRef. ⁴⁵. ^eRefs. ⁶¹⁻⁶³. ^fRef. ⁶⁴. ^gRefs. ^{51, 52}. ^hRef. ⁵³.

2.3. Surface Energy. In addition to lattice parameters, an equally critical property for validation are energy differences, which can be assessed using (hkl) surface energies, solvation, and adsorption data. ^{26, 30, 31, 35, 36, 42, 60, 84, 85} We benchmark surface energies, which are equal to cleavage energies for newly created surfaces from the bulk material, and largely determined by atomic charges and resulting Coulomb interactions. Freshly cleaved surfaces usually undergo some surface reconstruction after cleavage. ^{30, 31, 60, 84, 85} (Therefore, our definition of surface energy/cleavage energy differs from "surface energies" calculated from contact angle measurements that rely on already-cleaved and reconstructed surfaces.) Cleavage energies are reported for the lowest energy (hkl) surfaces of all compounds, which include (0001) surfaces of corundum-type oxides, (400) surfaces of oxides of rock-salt type, and the (0002) surfaces of the hydroxides, consistent with prior experimental and computational data. The (400) surfaces are often identified as (100) surfaces, and (0002) surfaces often as (0001) surfaces in prior literature, which is incorrect (too simplified) as a result of limited characterization at the atomic scale (see Computational Methods).

Experimental data for cleavage energies are available for several compounds (Table 6). Obtaining reliable values, however, has been challenging due to scarcity of data, inconsistencies in some measurements, as well as divergent definitions. A major goal in this work has therefore been to obtain consistent estimates with under 10% uncertainty. Towards this goal, we employed the analysis of known experimental data from diverse types of measurements, computational data with IFF, and chemical theory. We invoked analogies to known cleavage energies of chemically similar compounds such as clay minerals, sulfates, phosphates, and related oxides, ^{30, 31, 35, 42, 60, 68, 68} as well as data from multiple other calculation techniques, including high-level QM calculations,

(Table 6 and Table S2 in the Supporting Information). Quantum mechanical and other theoretical data^{65, 86-89} were hereby treated with appropriate caution. For example, various DFT flavors result in computed surface energies and adsorption energies on well-characterized metals and metal oxides that differ up to 100% from known experimental values, even when using dispersion-corrected density functionals, and were not used as a primary source of data.^{65, 90-93}

Specifically, the (0001) surface energies in the M₂O₃ group are relatively well supported for alumina (1.65 J/m²)^{94, 95} and iron(III)oxide (1.9 J/m²)^{96, 97} by consistent experimental data, related to each other by the same crystal structure, similar chemistry and atomic charges (Table 6). This analogy supports a suggested value for chromia of about 1.8 J/m². Some earlier calculation data are also found in this range (Table S1 in the Supporting Information). The surface energies of M₂O₃ oxides with a metal oxidation state of +3 and atomic charges of 1.6e to 1.7e are furthermore expected to be higher than those of the MO oxides, which have an oxidation state of +2 and lower atomic charges of 1.1e to 1.2e (Table 6). Surface energies hereby scale approximately with the square of the atomic charges. Accordingly, the (400) surface energies in the group of MgO, CaO, and NiO oxides are in the range of 0.7 to 1.0 J/m². Herein, the (400) surface energy of MgO is well supported to be 1.0 J/m² by multiple laboratory measurements at room temperature, ^{98, 99} and was recorded as 0.71 J/m² at the melting point of 3125 K.¹⁰⁰ The surface energy for CaO is expected to be somewhat lower, and NiO similar to MgO, based on some differences in lattice parameters and bonding, ¹⁰¹ as well as according to atomic charges from the Extended Born model. ⁴¹ Extensive experimental reference data are available for surface tension measurements of molten CaOcontaining mixed oxides and slag, which indicate 0.65 J/m² at 1700 K.¹⁰² The surface energy of a solid at 298 K is always higher than the surface tension of a high temperature melt, ¹⁰³ in proportion to the temperature difference, and suggests a cleavage energy on the order 0.7-0.8 J/m² for CaO at room temperature (Table 6). Several calculations agree with this range, and with slightly larger values for NiO (Table S1 in the Supporting Information). Older reported values for the surface energy of CaO of 1.3 J/m² are clearly too high.¹⁰⁴

The M(OH)₂ hydroxides result from hydration of the oxides and have a layered structure. The (0002) plane is of lowest cleavage energy. Hydroxide ions are present on both sides of the newly created surfaces, and the surface energy is expected to be on the order of magnitude of the surface tension of water (72 mJ/m²)⁶⁷ due to hydration and similar hydrogen bonding. The hydroxide ions have a higher polarity compared to OH groups in water, represented by larger negative oxygen atomic charges (between -1.32e and -1.02e compared to -0.82e in water), plus some variation in O-H bond length and H atomic charge (+0.3e to +0.5e compared to +0.41e in water). Therefore, cleavage energies are in a range of 0.15 to 0.25 J/m², which is higher than the surface tension of water (0.072 J/m²), and in a similar range as alkali and earth alkali halides (0.15 to 0.25 J/m²).⁴¹, ¹⁰⁵⁻¹⁰⁸ Several earlier simulation data support values in this range of (Table 6 and Table S1 in the Supporting Information). The IFF models of oxides and hydroxides were calibrated to best reproduce these likely surface energies, consistent with the known atomic charges and LJ parameters relative to validated compounds with similar chemistry. Agreement in computed lattice parameters and bulk moduli with experimental data (Table 7 and next section) supported convergence on the most likely values for the cleavage energy.

In summary, the best estimates of the surface energies are based on experimental results and some help of theory. We used these values to benchmark the performance of IFF models and other atomistic models (Table 6). Furthermore, we tested the surface energies of various (hkl) surfaces with IFF, which confirmed that the (hkl) surfaces of lowest energy are the (0001) surfaces of M₂O₃-type oxides, the (400) surfaces for MO type oxides, and the (0002) surfaces of M(OH)₂-type

hydroxides. The lowest computed surface energies for α -Al₂O₃, α -Cr₂O₃, and α -Fe₂O₃ are 1.64-1.68 J/m², 1.69-1.75 J/m², and 1.88-1.91 J/m², respectively (Table 6). For MgO, CaO, and NiO we obtained 0.85-0.9 J/m², 0.71-0.76 J/m², and 0.97-0.99 J/m², respectively. The computed cleavage energies of the hydroxides β -Mg(OH)₂, β -Ca(OH)₂ and β -Ni(OH)₂, are 0.19-0.26 J/m², 0.16-0.21 J/m², and 0.25-0.31 J/m², respectively. The statistical uncertainty in the computation was hereby \pm 0.01 J/m².

On average, computed cleavage energies with IFF for the low energy surfaces ((0001) in M2O3 oxides, (400) in MO oxides, and (0002) in hydroxides) deviate by about 7% from best-estimate reference data, while other force fields that routinely neglect such critical validation have average errors between 45% and 75%, or do not allow the simulations of surfaces and interfaces by default (Table 1 and Table 6). Specifically, the Pedone potential could not be used due to difficulties in implementation. The randomness of computed surface energies in other computational methods is notable: some cleavage energies even have a negative sign, which equates to voluntary decomposition of the bulk material, such as chromia in ReaxFF and the hydroxides in UFF. Since cleavage (or surface) energies directly scale with the ability of a force field to reproduce Coulomb and van-der-Waals energies combined, defect energies, adsorption in multiphase materials, ²⁶ and the ability to study catalysts for sustainability, ⁵⁶ the performance of IFF exceeds that of other force fields and of some flavors of DFT by a large margin. The highest deviation for any compound in any flavor of IFF (CVFF, CHARMM, AMBER, OPLS, PCFF/COMPASS) is 20%, compared to a minimum of 85% with other models (Table 6).

Notably, we required human effort to evaluate and interpret reference data in combination with tests by simulations and a low number of interpretable force field parameters. Automation and machine learning (ML) are still challenging to incorporate into this workflow since targeted

searches for reference data, evaluations of the quality of both reported techniques and measurement data, cross-checks to chemically similar compounds, and interpretations in the context of chemical theory require multi-domain expert knowledge and iterative processes beyond current ML capabilities. For example, if the wrong data were chosen and key rationales not followed, the deviations can be 4 to 5 times higher, and the practical value of resulting simulations with 40% to 50% error would be questionable.

and other computational methods (atomistic simulations and QM). In the column "Experiment", we list (1) best estimates including the uncertainty for each compound, and (2) individual measurements. Best estimates are based on experimental data, chemical analogy to Table 6. Comparison of the surface energy according to experimental data with calculated values in this work (IFF 12-6 LJ and 9-6 LJ) similar oxides, our prediction, and QM data. Deviations of computed values relative to the best estimates are stated for each compound.

	_				
Other comput. (DFT) ⁿ	1.00-5.32	-39% to 222%	1.61, 2.95	-11%, 64%	1.53, 2.1
UFF ^m	NP	NP	NP	NP	NP
ClayFF ¹	1.11	-33%	NA	NA	1.60
ReaxFF ^j	$1.07, 1.00^{k}$	-35%, -39%	-0.13	-107%	2.89
Pedone ⁱ		pəındu	l not be cor	Could	
IFF- PCFF- HQ	1.66	%9.0	1.73	-4%	1.91
IFF- PCFF	1.64	-0.6%	1.69	%9-	1.88
IFF- CHARMM, AMBER	1.67	1%	1.74	-3%	1.91
IFF- CVFF, OPLS	1.68	2%	1.75	-3%	1.89
Experiment	1.65 ± 0.1 $1.57^{a}, 1.69^{b},$ 2.6^{c}	Dev from best est.	1.8 ±0.1 NA	Dev from best est.	1.9 ± 0.1 1.9^{d}
Surface energy (J/m²)	α-Al ₂ O ₃ (0001)		α -Cr ₂ O ₃ (0001)		α -Fe ₂ O ₃ (0001)

-19%, 11%	1.02-1.36	7% to 43%	0.61-1.03	-19% to 37%	0.38-2.67	-64% to 154%	NA
N	0.22	-77%	0.27	-64%	NP	N	0 VI
-16%	1.27	34%	0.53	-29%	NA	-NA	0.41
25%	2.41	154%	0.63	-16%	0.40	-62%	0.39
0.5%	06.0	-5%	0.76	1%	66.0	%9-	0.26
-1%	0.85	-11%	0.71	-5%	0.94	-10%	0.24
0.5%	0.86	%6-	0.72	-4%	76.0	-7%	0.19
0.5%	0.87	%8-	0.72	-4%	0.97	-7%	0.23
Dev from best est.	0.95 ± 0.05 $1.04^{e}, 1.0^{e},$ $1.05^{f}, 0.53$ 0.71^{g}	Dev from best est.	0.75 ± 0.05 $1.31^{g}, 0.52$ 0.85^{g}	Dev from best est.	1.05 ± 0.05 NA	Dev from best est.	0.225 ±0.025 NA
	MgO (400)		CaO (400)		NiO (400)		β -Mg(OH) ₂ (0002)

NA	0.107, 0.114	-39%, -35%	0.201	-27%
-100%	0 VI	-100%	0 VI	-100%
82%	0.37	85%	NA	NA
73%	0.17	-3%	0.93	238%
16%	0.21	20%	0.31	13%
7%	0.19	%6	0.29	5%
-16%	0.16	%6-	0.25	%6-
2%	0.19	%6	0.27	-2%
Dev from best est.	0.175 ± 0.025 1.18^{h}	Dev from best est.	0.275 ±0.025 NA	Dev from best est.
	β-Ca(OH) ₂ (0002)		β-Ni(OH) ₂ (0002)	

^aRef. ⁹⁴. ^bRef. ⁹⁵. ^cRef. ^{109, 110}. ^dRef. ^{96, 97}. ^eRef. ⁹⁸. ^fRef. ⁹⁹. ^gRefs. ^{100-102, 111} (based on surface tension of molten solid). ^hRef. ¹¹¹. ⁱRef. 45. j Ref. 61-63. k Ref. 64. l Ref. 51, 52. m Ref. 53. n See Table S1 in the Supporting Information for details including all specific references. NA = Not available, NP = Not possible due to bonded model. When using UFF, hydroxides have repulsive interactions and the simulation box is unstable.

2.4. Bulk Modulus. Computed bulk moduli, as a measure of mechanical properties and 2nd derivatives of the energy, deviate on average 5% from experimental data when using 12-6 LJ potentials in IFF (CHARMM, CVFF, AMBER, OPLS-AA) (Table 1, Table 7). Average deviations increase to 21% when using 9-6 LJ potentials (PCFF/COMPASS) unless atomic charges are increased (PCFF-HQ) (Table 1, Table 2). The necessity for modifications in the case of the 9-6 LJ potential shows that 12-6 LJ potentials provide an overall better representation of the physical interactions, which was similarly observed for metals^{27, 112} and several minerals.^{26, 42}

Experimental reference values for the bulk modulus of oxides and hydroxides have been readily available, and we analyzed between 3 and 13 independent measurements for each compound (Table S3 in the Supporting Information for full compilations). Accordingly, the bulk moduli of the corundum type oxides Al₂O₃, Cr₂O₃ and Fe₂O₃ are 254±3 GPa, 231±5 GPa and 241 ± 8 GPa, respectively, which feature only small uncertainties between $\pm1\%$ and $\pm3\%$ (Table 7). The high moduli are related to the comparatively high atomic charges (Table 2) and surface energies (Table 6). Bulk moduli are reproduced almost within the experimental uncertainty by IFF (Table 7). The rocksalt-type oxides MgO, CaO and NiO have bulk moduli of 160±5 GPa, 115±3 GPa, and 200±11 GPa, which are somewhat lower than those for the M₂O₃ oxides and reproduced by IFF largely within the experimental uncertainty of $\pm 3\%$ to $\pm 5\%$ as well (Table 7). The hydroxides Mg(OH)₂, Ca(OH)₂, and Ni(OH)₂, as products of the hydration reaction of the oxides, have expectedly lower bulk moduli of 45±6 GPa, 35±6 GPa, and 55±6 GPa, respectively. Even though many laboratory measurements are available (Table S2 in the Supporting Information), the uncertainty in the reported bulk moduli for the hydroxides is quite high, between $\pm 11\%$ and $\pm 18\%$, and computed values from IFF stay within these bounds (Table 7). Interestingly, the scatter in

computed values for specific IFF energy expressions (CHARMM/AMBER, CVFF/OPLS-AA, PCFF/COMPASS) was also larger than for the corresponding oxides.

Among alternative potentials, the Pedone force field yields the same accuracy for bulk moduli as IFF, however, it cannot include interfaces with solvents and organic compounds. ClayFF, ReaxFF, and UFF yield much higher average errors in bulk moduli of 24%, 44% and even 445%, respectively. ReaxFF and UFF can be particularly unreliable with individual deviations of more than 100% or even 1000% (Table 7).

The 12-6 LJ potential in IFF fares better than the 9-6 LJ potential overall. Typically, we use the same atomic charges for 12-6 and 9-6 LJ functional forms as they represent the same chemical identity (electron distribution) in a material. However, the nonbonded potentials do not include bonded terms as a simplification, which results in a lower bulk modulus by 7% to 30 % with the 9-6 LJ potential when using the same charges as in the 12-6 LJ potential. As an alternative, we derived a second set of LJ 9-6 models, IFF-PCFF-HQ, with higher atomic charges (Table 2). The IFF-PCFF-HQ parameters match the experimental bulk modulus within 10 % of the experimental values, along with excellent performance for lattice parameters and surface energy. Hereby, the higher charges artificially compensate for weaker bond strength when using a LJ 9-6 potential, which has a softer repulsive component to keep bonds lengths near equilibrium compared to the 12-6 LJ potential.

Table 7. Comparison of the bulk modulus according to experiments, calculations with IFF (12-6 LJ and 9-6 LJ options), and other computational methods (Pedone et al, ReaxFF, ClayFF, and UFF). Values in brackets indicate the deviation relative to experiments. Computational values have an average statistical uncertainty of ±4 GPa.

Bulk modulus (GPa)	Expt.ª	IFF- CVFF, OPLS	IFF- CHARM, AMBER	IFF- PCFF	IFF- PCFF- HQ	Pedone ^b	ReaxFF ^c	ClayFFe	UFFf
α -Al ₂ O ₃	254 ± 3	274	255	207	235	275	41, 248 ^d	194	552
	Dev from expt	%8	0.4%	-19%	-7%	%8	-84%, -2 %	-24%	106%
α -Cr ₂ O ₃	231 ± 5	241	233	190	224	237	237	NA	515
	Dev from expt	4%	1%	-18%	-3%	3%	3 %	NA	123%
α -Fe ₂ O ₃	240 ± 8	250	248	201	231	229	261	124	2675
	Dev from expt	4%	3%	-16%	-4%	-5%	%6	-48%	1015%
MgO	160 ± 5	161	166	123	150	168	356	225	30
	Dev from expt	%9.0	4%	-23%	%9-	2%	123%	41%	-81%
CaO	115 ± 3	114	122	103	109	120	40	143	38
	Dev from expt	-1%	%9	-10%	-5%	4%	-65%	24%	-67%

2755	1278%	Unstable	Unstable	Unstable	Unstable	Unstable	Unstable
NA	NA	43	-4%	36	3%	NA	NA
18	-91%	51	13%	27	-23%	42	-24%
193	-4%	NA	NA	NA	NA	NA	NA
186	-7%	39	-13%	32	%6-	52	-5%
139	-31%	35	-22%	24	-31%	44	-20%
188	%9-	48	7%	39	11%	57	4%
193	-4%	44	-2%	31	-11%	53	-4%
200 ± 11	Dev from expt	45 ± 6	Dev from expt	35 ± 6	Dev from expt	55 ± 6	Dev from expt
NiO		β -Mg(OH) ₂		β -Ca(OH) ₂		$\beta\text{-Ni(OH)}_2$	

^a We utilized extensive experimental reference data for the bulk modulus, between 3 and 13 references for each compound. The original references, individual values, and best estimates for each compound are listed in Table S2 in the Supporting Information. ^b Ref. ⁴⁵. NA = Not available. c Refs. 61-63. d Ref. 64. e Refs. 51,52. f Ref. 53. All structures can be built and subjected to calculations, however, fluctuations can be high and the dynamics often appears unphysical. Next, we will illustrate how IFF parameters are suited to compute properties not included in the derivation protocols, such as lattice parameters of mixed oxides, free energies of ion migration in oxides, and adsorption energies of water and organic molecules within $\sim 10\%$ of experimental measurements.

2.5. Application to Mixed Oxides. The IFF models can be used to simulate mixed oxides, glasses, defects, electrolyte interfaces, organic hybrid materials, interfaces with metals, 2D materials, and large biomacromolecules. We demonstrate four example applications to mixed oxides such as spinel (MgAl₂O₄) (Figure 3a-c), defects and migration barriers of Ca²⁺ and Ni²⁺ in CaO and NiO (Figure 3d-f), as well as the binding energy of water and organic molecules on MgO (100) surfaces in comparison to experimental data (Figures 4, 5, and Table 8). An unlimited space of bulk materials and interfaces can be studied and validated in follow-on studies.

Mixed oxides can form upon synthesis from the melt, from solution precursors, or at the interface of metal alloys and oxide films during oxidation or corrosion. As an example, spinel structures such as MgAl₂O₄ can form from rock salt (MgO) and corundum (α-Al₂O₃). Some spinel-type minerals have great potential in catalysis, for example, in the oxygen evolution reaction in water splitting.¹¹³ We used the crystal structure of MgAl₂O₄ from AMCSD^{75, 114} and the parameters of the two component oxides as is to simulate the density, lattice parameters, and bulk modulus (Figure 3a, b). Only a small adjustment of the O charge was made to maintain overall charge neutrality (charge neutrality is always necessary). The coordination number of Al remains at 6 while the Mg coordination number with oxygen changes from 6 in MgO to 4 in MgAl₂O₄. The calculated density with the oxide parameters of Mg, Al and O was 3.492 g/cm³ and deviates from the experimental value¹¹⁴ of 3.570 g/cm³ by only -2.2% (Figure 3a, b, Sim. 1). The computed bulk modulus of 201 GPa agrees perfectly with experimental data of 200 GPa, given ~3%

uncertainty.¹¹⁵ The deviation in atomic positions can hardly been seen (Figure 3b). The deviation in lattice parameters of +0.7% is larger than those for IFF core compounds, although it is still better than other fitted force fields and common density functionals (Table 1). Accordingly, in Simulation 1 the atomic charges remained at +1.06e for Mg, +1.62e for Al, and -1.075e for O (balanced between -1.06 and -1.08e for charge neutrality), and the LJ parameters (r_{min} and ε) 2.06 Å and 0.4 kcal/mol for Mg, 1.72 Å and 0.45 kcal/mol for Al, and 3.3 Å and 0.35 kcal/mol for O (Table 2).

In Simulation 2, we tested small modifications of the parameters to improve the fit, if desired (Figure 3a, c, Sim. 2). Hereby, we lowered the charge of Mg from 1.06e to 0.96e, changed r_{min} for Mg from 2.06/0.4 to 1.93 Å/0.4 kcal/mol, and modified the oxygen charge to -1.05e to maintain overall charge neutrality. The lower charge (and less repulsive r_{min}) of Mg reflects the lower coordination number of 4 in the interstitial sites (as opposed to 6 in MgO).⁴¹ This adjusted parameter set matches lattice parameters with 0.1% deviation and the bulk modulus remains at 0.5% deviation from experimental data (Figure 3a, c, Sim. 2). All other parameters remain the same (Al: 1.62e, 1.72 Å and 0.45 kcal/mol; O: -1.05e, 3.3 Å and 0.35 kcal/mol). These minor adjustments, which physically reflect the change in Mg coordination number and its effect on atomic charges (smaller) and atomic radius (smaller due to less repulsion at lower charge), show that the simulation of other oxide composition is straightforward (Figure 3a, b, Sim. 1). If any changes are desired for the best fit, they are minor and interpretable, i.e., on the order of 10% in atomic charges and LJ parameters (Figure 3a, c, Sim. 2). The conditions are that (1) overall charge neutrality must be maintained, (2) changes in charges and LJ parameters, if desired, follow expected changes in coordination environments.

2.6. Application to Ion Migration. The growth of oxide films on metal surfaces upon oxidation and corrosion happens via cation migration. As an example, the nonbonded models of

CaO and NiO were used to compute the free energy of cation migration using steered molecular dynamics simulations. As the migration takes place, the free energy was plotted as a function of distance (Figure 3d, e), whereby one cation was pulled from one atomic layer to a cation vacancy in the next atomic layer (Figure 3f). The Ni²⁺ or Ca²⁺ cations were moved at a rate of 1 Å/ns, and any slower rates yield convergent results. The cation migration barrier is reported as an average of the forward and reverse barriers. The computed free energy barriers for Ca⁺ and Ni⁺ ions are 31 kcal/mol and 32 kcal/mol respectively, which agree very well with the experimentally reported barriers of 34-36 kcal/mol for Ni²⁺ ions¹¹⁶⁻¹¹⁹ and 28-34 kcal/mol for Ca²⁺ ions (Figure 3d-f).¹²⁰, 121 The results show a near perfect match that exceeds the performance of common DFT simulations at a million times lower cost. To carry out these simulations, two vacancies at a distance greater than 60 Å were created by deleting a metal cation and an oxygen anion from the crystal model of ~80x80x80 Å³ size to maintain charge neutrality, equal to a Schottky defect (Figure S1 in the Supporting Information). The cation vacancy was placed at the center of the crystal and the anion vacancy was generated at the origin of the crystal system to minimize interaction between the two vacancies and obtain unbiased cation migration free energies.

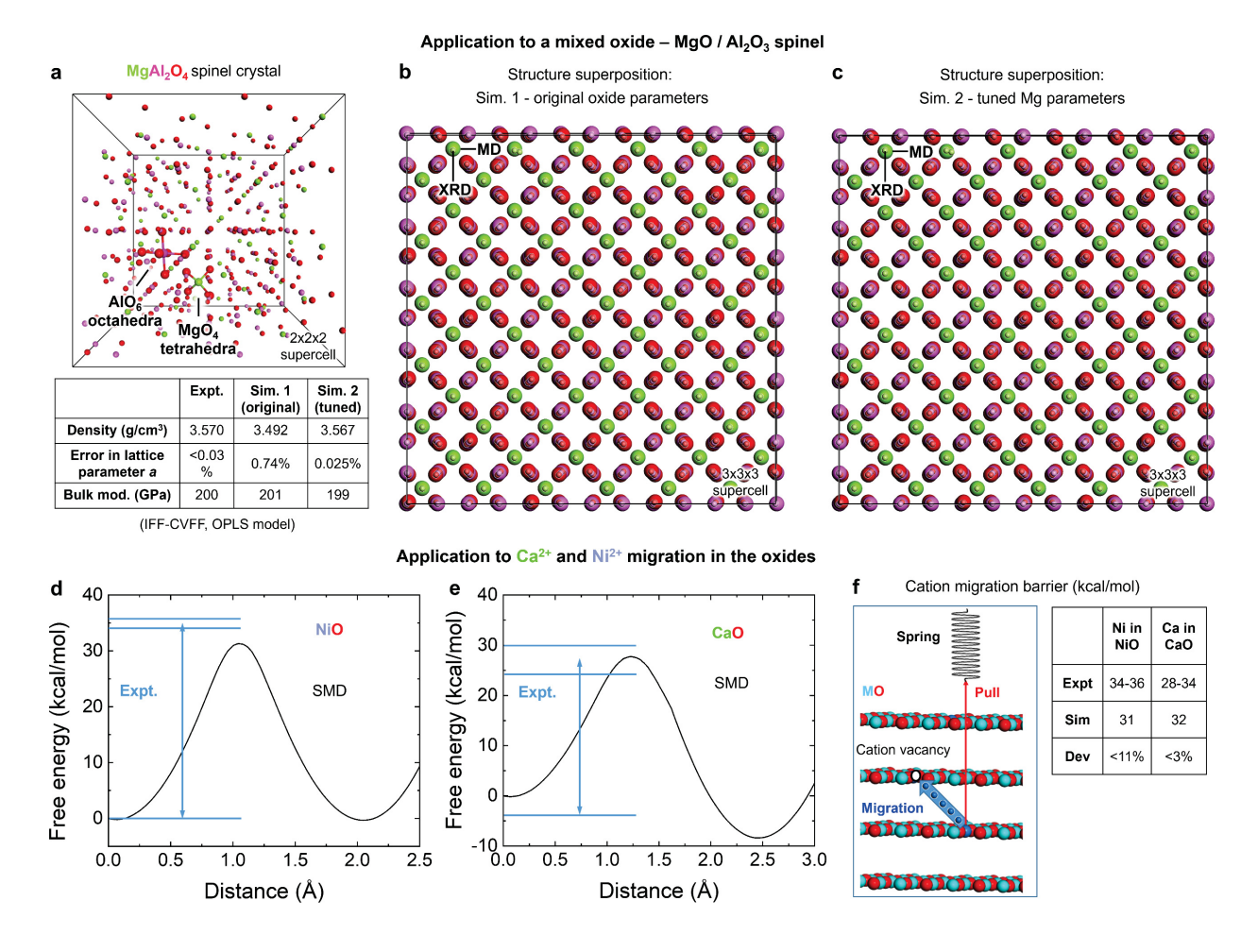


Figure 3. Application of the IFF models to mixed oxides and cation migration. (a) The supercell of spinel, MgAl₂O₄, and comparison of the density, lattice parameters, and bulk modulus from experiments versus simulation with IFF. Two models are compared, including one with the original unmodified oxide parameters (Sim. 1) and slightly modified parameters for MgO to better match tetrahedral coordination and the density (Sim. 2). The agreement of lattice parameters is very good, under 1% deviation without parameter modifications, and the bulk modulus matches experimental data within the measurement uncertainty (~3%) with both models. The octahedral coordination environment of Al and the tetrahedral coordination of Mg are highlighted. (b) Overlay of the crystal structure of spinel from XRD (smaller spheres) with that obtained by MD simulation using original oxide parameters (Sim. 1, larger spheres). The offset is small and barely

visible. (c) Overlay of the crystal structure of spinel from XRD (smaller spheres) with that obtained by MD simulation using the tuned oxide parameters (Sim. 2, larger spheres). The structures match almost perfectly. (d) Free energy profile of Ni²⁺ cation migration from one layer to the next layer in NiO (which contains a vacancy) in steered molecular dynamics simulation. The free energy as a function of reaction coordinate is also called "potential of mean force". (e) Free energy profiles of Ca²⁺ cation migration from one layer to the next layer in CaO, which contains a vacancy, in steered molecular dynamics simulation. (f) Schematic of steered molecular dynamics simulation used to migrate a cation from one layer to the vacancy in the next layer along with a comparison of the experimental and computed free energy of migration and deviation. A comparison of the computed free energy barriers to experimental data shows average deviations under 10%, close to the measurement uncertainty (table at right hand side). The pulling speed was 1 Å/ns.

2.7. Application to Mineral-Water and Mineral-Organic Interactions. The nonbonded models were further tested to compute the adsorption energy of water and organic molecules on the MgO (400) surface, often simplistically called a (100) surface, for which experimental reference data are available. We used IFF and CVFF, OPLS format, the flexible SPC water model, which can be replaced with TIP3P water with <5% changes in computed properties, ^{30, 58} and the CHARMM36 parameters for organic molecules. ¹²² The computed adsorption geometry of single water molecules on MgO (400) surfaces at 0 K agrees with quantum mechanical results, and the computed adsorption energy of -10.8 kcal/mol closely matches -11.3 kcal/mol obtained from highlevel CCSD(T) quantum mechanical calculations (Figure 4a). ^{66, 123} Other quantum methods at MP2 and CPC-CBS(D, T) levels indicate -10 to -12.7 kcal/mol, and DFT-D2 up to -15 kJ/mol, which is quite significantly lower accuracy compared to IFF. ⁶⁶ Molecular dynamics simulation of single

water molecules at a low temperature of 170 K yields an adsorption enthalpy of -8.4 kcal/mol, which is within the range of experimental measurements of -8.6 to -12 kcal/mol (Figure 4b). 124 Laboratory data are based on adsorption isotherms measured for temperatures between 100 K and 300 K for equal surface coverage, as determined by low energy electron diffraction (LEED) and helium-atom scattering (HAS). 124, 125 Under these conditions and at low surface coverage, reversible physisorption of isolated water molecules was observed.^{66, 126} Typical molecular conformations from MD simulations indicate that a reaction to Mg(OH)₂ could easily proceed via dissociation of an OH bond in adsorbed water (side view in Figure 4b). Binding enthalpies of water at monolayer coverage at 170 K were calculated as -15.2 kcal/mol, using 50 H₂O molecules on a 21.05 x 21.05 Å² cross-sectional area, which compares to laboratory measurements of -20.3 kcal/mol (Figure 4c). 124, 125 According to spectroscopic studies, water partially dissociates on MgO (400) surfaces and forms a layer with both water molecules and OH groups at intermediate and monolayer coverage, ^{127, 128} which adds an exothermic reaction enthalpy up to -9.0 kcal/mol (930 J per g MgO). 129, 130 The computed adsorption enthalpy of -15.2 kcal/mol for undissociated water is thus in good agreement with the experimental data of -20.3 kcal/mol, assuming that dissociation of one third of water molecules¹²⁶ would add -3 kcal/mol for the partially dissociated water layer in experiment. The position and orientation of adsorbed water molecules at monolayer coverage in the MD simulation also follow closely the observations in LEED and HAS, which indicate the existence of several partially ordered water networks (Figure 4c top view and below). Hereby, the oxygen atoms in water coordinate with magnesium ions of the MgO surface. Overall, the simulation of physisorbed water using IFF appears realistic with respect to binding geometries and ~10% uncertainty in binding energies.

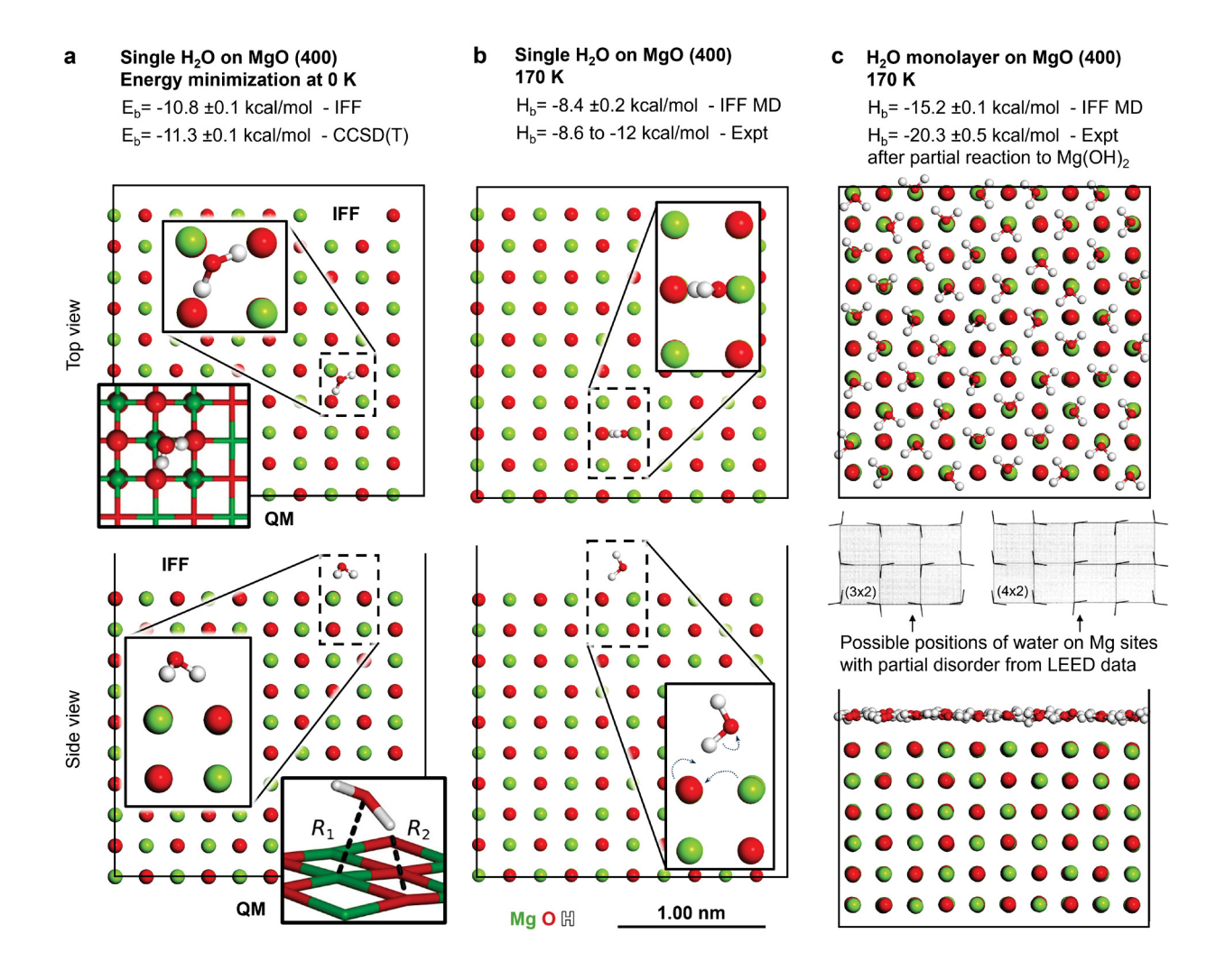


Figure 4. Application of the IFF MgO oxide models to analyze binding of water molecules to the MgO (004) surface using geometry minimization and molecular dynamics simulations. The IFF-CVFF, OPLS model was used along with the flexible SPC water model. (a) Geometry optimization, equal to energy minimization at 0 K, of single water molecules yields a binding geometry similar to those observed in quantum mechanical MP2 and CCSD(T) calculations (insets in top and side views). ^{66, 123} The IFF binding energy deviates less than 5% from the CCSD(T) value. ⁶⁶ (b) Molecular dynamics simulations at 170 K show representative orientations of single water molecules. The computed binding enthalpy is in the range of experimental data. ¹²⁴ The orientation is favorable for dissociation into hydroxide ions (necessary shifts in electron density

are indicated by dotted arrows). ^{127, 128} (c) Monolayer adsorption at 170 K indicates locally ordered orientations of water molecules, similar to structures from LEED measurements indicated between the top and side views. ¹²⁵ The computed binding enthalpy of water is 5 kcal/mol weaker than in experimental measurements, which involves partial dissociation into hydroxide ions ¹²⁶⁻¹²⁸ with an exothermic reaction enthalpy of -9.0 kcal/mol per dissociated water molecule. ^{129, 130} The overall agreement between computation and experiments is very good.

More detailed validation is possible for the adsorption of organic molecules on the MgO (400) surface. Hereby, reactions do not occur and measurements of the adsorption energy are available for multiple molecules from temperature-programmed desorption (TPD) (Figure 5 and Table 8). 131, ¹³² Measurements were carried out close to monolayer coverage, and accordingly we analyzed the adsorbed configurations of C₂H₆, n-C₄H₁₀, and n-C₈H₁₈ for half a monolayer (0.5 ML) and for full monolayer coverage (1 ML) on a Mg (400) slab in equilibrium (Figure 5a-f). Monolayer coverage was achieved for 204, 109, and 65 molecules of C₂H₆, n-C₄H₁₀, and n-C₈H₁₈, respectively, using an MgO (400) surface area of 63.165 x 63.165 Å² (Table 8). The computed adsorption energies for 1 ML coverage with C₂H₆, n-C₄H₁₀, and n-C₈H₁₈ on MgO surface were -6.0 kcal/mol, -9.6 kcal/mol and -18.0 kcal/mol (Table 8). The computed values for 0.5 ML coverage are approximately 5% lower at -5.7, -9.1, and -17.1 kcal/mol. The agreement with experimental data from TPD measurements, which are -5.4, -8.5, and -15.2 kcal/mol, respectively, is between 8% and 13%. The agreement is very good given ~10% uncertainty from TPD measurements, no use of any fitting parameters for the interfaces, and using CHARMM36 parameters for the organic molecules which have some uncertainties of their own. DFT calculations, which are not feasible

for systems this size including dynamics, often have uncertainties of 50% and higher for small molecules, depending on the density functional. 65, 92, 93, 133, 134

Similar agreement of computed and experimentally measured adsorption energies and conformations of organic molecules, biopolymers, and gases on nanostructured metals, minerals, and 2D materials on the order of 10% or better was previously demonstrated using IFF parameters and combinations with CHARMM, AMBER, OPLS-AA, PCFF, and other (bio)organic force fields. 25, 29, 30, 34-36, 56, 57, 59, 135, 136

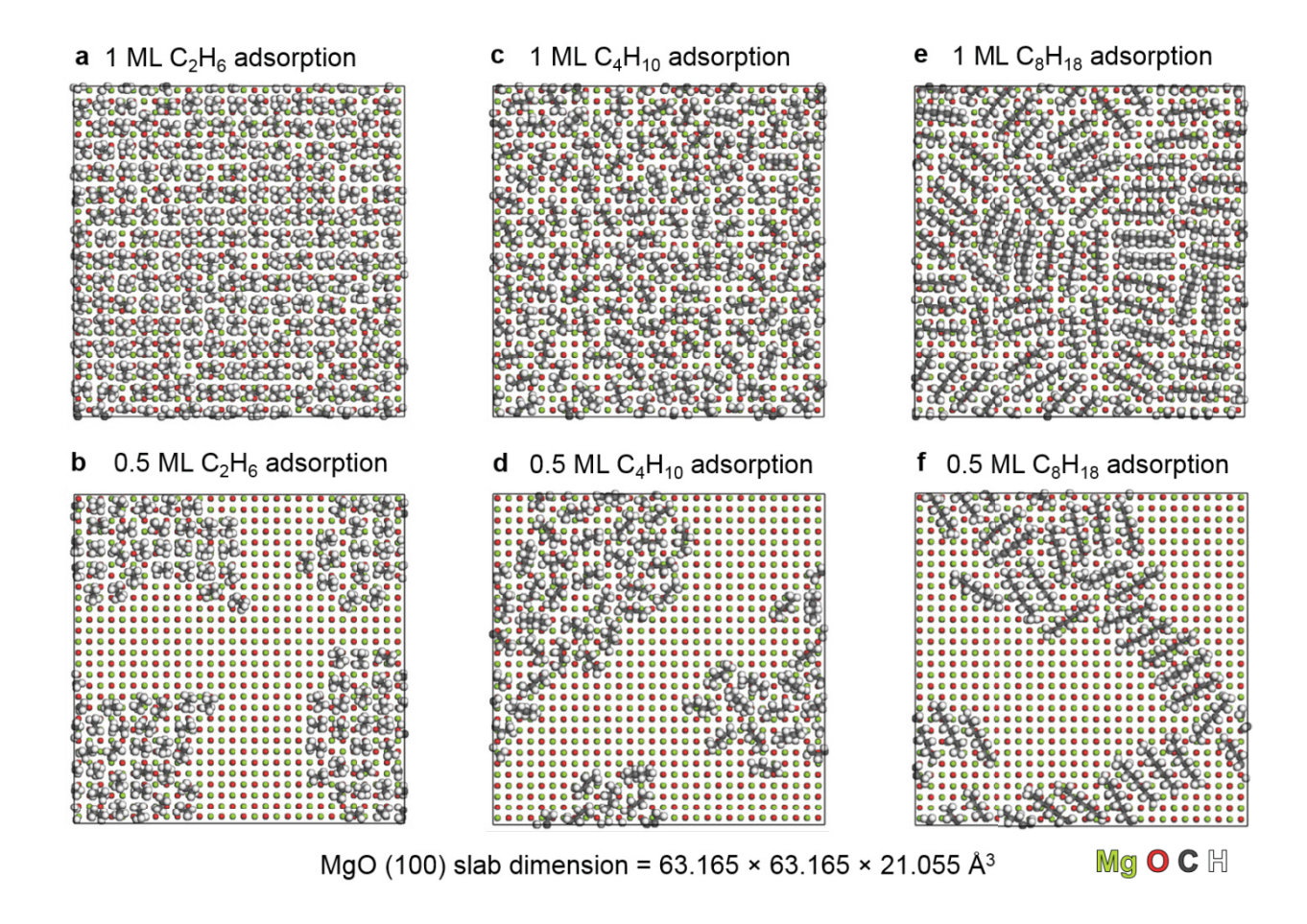


Figure 5. Application of the IFF MgO oxide models to analyze alkane binding to the MgO (004) surface using molecular dynamics simulations. (a) Snapshot of equilibrium adsorption of C₂H₆ at 1 monolayer (ML) surface coverage. (b) Adsorption of C₂H₆ at ½ ML coverage. (c) Adsorption of n-C₄H₁₀ at 1 ML surface coverage. (d) Adsorption of n-C₄H₁₀ at ½ ML coverage. (e) Adsorption of n-C₈H₁₈ at 1 ML surface coverage. (f) Adsorption of n-C₈H₁₈ at ½ monolayer (ML) coverage. Fractional coverage leads to nucleation of islands on the surface. At full coverage, the formation of domains with different orientation can be seen as the chain length increases.

Table 8. Adsorption energy of C₂H₆, n-C₄H₁₀, and n-C₁₀H₁₈ on the Mg(004) surface according to experiments^{131, 132} and MD simulations for surface coverages of 1.0 and 0.5 monolayer coverage.

Approximate uncertainties for the experimental measurements and statistical uncertainties for the simulation results are indicated.

Alkane	Type of measurement	Surface coverage	N ^a	Adsorption energy E _a (kcal/mol)
C ₂ H ₆	Expt	Near 1 ML	I	-5.4 ± 0.5
	Simulation	1 ML	204	-6.0 ± 0.5
	Simulation	½ ML	102	-5.7 ± 0.5
C_4H_{10}	Expt	Near 1 ML		$\textbf{-8.5} \pm \textbf{0.8}$
	Simulation	1 ML	109	-9.6 ± 0.5
	Simulation	½ ML	54	-9.1 ± 0.5
$\mathrm{C_8H_{18}}$	Expt	Near 1 ML		-15.2 ± 1.5
	Simulation	1 ML	65	-18.0 ± 0.5
	Simulation	½ ML	32	-17.1 ± 0.5

^a Number of molecules on the surface.

Simulations of biomolecule-oxide and biomolecule-hydroxide assemblies in solution use the same type of models as for water and organic molecules and are expected to perform with similar accuracy. As shown in prior work, IFF is well suited to characterize peptide and protein interactions with various minerals.^{29, 31, 35, 36, 137, 138} Molecular geometries typically agree with

experimental reference data within ~0.5%, plus tolerances depending on the reliability of the biomolecular parameters (1% to 3%). Computed binding energies usually agree on the order of ±10% with experimental data, and sometimes better. The expected accuracy specifically correlates with the values for surface energies (Table 6).²⁶ Proof-of-concept simulations for biomolecule-oxide and biomolecule-hydroxide assemblies can be carried out in future studies as they require significant effort and only qualitative experimental reference data are currently available. For example, experimental studies of peptide binding to some oxides and hydroxides were summarized in ref. ¹³⁹, such as preferred binding of the peptide QMDTSTSLAPSR and non-preferred binding of the peptide HANHQAWNNLA to hematite, α-Fe₂O₃. ¹⁴⁰ Specific adhesion of *Escherichia coli* bacteria to iron oxide nanoparticles and potential recognition motifs such as RRTVKHHVN at pH 8 have been suggested by laboratory studies. Going forward, quantitative analysis from the molecular scale to the small cellular scale using MD simulations with IFF models and experiments could answer numerous questions related to molecular recognition, the function of nanoparticle therapeutics, imaging agents, vaccine adjuvants, and potential mechanisms of toxicity.

2.8. Surface Reconstruction. The creation of surfaces by cleavage, as compared to the bulk crystal, leads to changes in electrostatic interactions at the surface layers and surface reconstruction. $^{31, 60, 84, 85}$ In case of α -Al₂O₃, the bulk structure can be described as a sequence of two layers of Al-atoms followed by a layer of O atoms (Figure 6a, b). Creation of the (0001) surface of lowest energy involves cleavage between the two Al layers, which are then distributed on either side of α -Al₂O₃ slab. Due to changing electrostatic interactions, namely, the absence of neighboring Al atoms and O atoms, the surface Al-atoms move closer to the underlying O-layer (Figure 6a, b). In addition, the 2 Al layers below the top O-layer merge together (middle arrow

Figure 6a, b and inset of Figure 6b) while the two Al peaks remain distinct in the bulk (Figure 6a, b).

In the structure of rock salt type, the atomic layers are composed of both cations and anions in alternation as shown for MgO (Figure 6c, d). In this structure, both metal and oxygen atoms are equally exposed on the low energy (004) surface, cleavage is electroneutral by default, and virtually no surface reconstruction is observed.

The hydroxide (0002) surfaces are terminated with hydroxide ions and the bulk structure consists of a repeat sequence of a layer of (HO) groups, followed by a layer of metal atoms, followed again by an (OH) layer as depicted for β -Ni(OH)₂ (Figure 6e, f). Virtually no reconstruction of (0002) surfaces is observed due to fully electroneutral cleavage between adjacent (OH) layers and loss of comparatively weak electrostatic interactions between the 2 hydroxide layers. All atoms were mobile during the simulations of cleavage to analyze the surface dynamics.

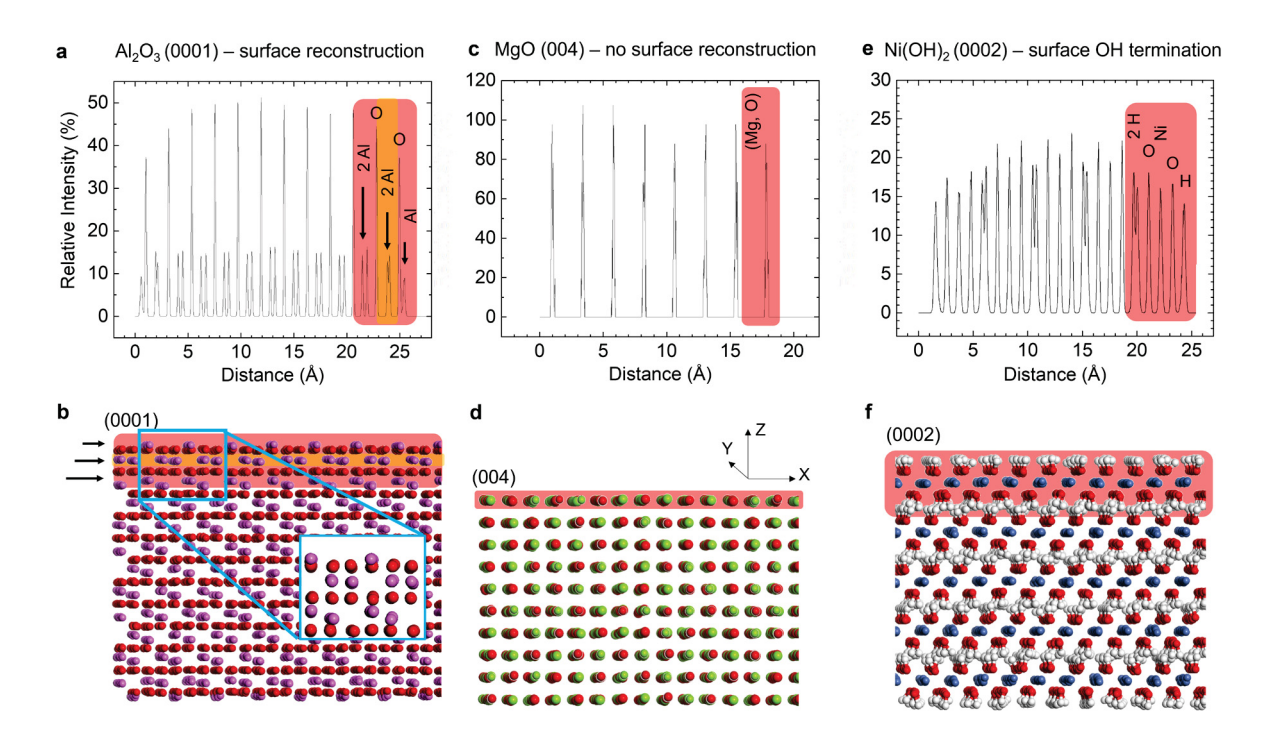


Figure 6. Sequence of atomic layers and surface reconstruction in the oxides and hydroxides. (a) The density profile of the α -Al₂O₃ (0001) surface shows discrete atomic layers of Al and oxygen. The top three Al-containing atomic layers near the surface are marked by arrows. The superficial Al layer moves closer to the O layer below than in the bulk structure (red highlight). The next two Al atomic layers towards the bulk tend to unite into one peak (red highlight) compared to two separate peaks for Al atomic layers further inside (red highlight). (b) Side view of the α-Al₂O₃ (0001) surface, which matches the density profile in (a). The inset shows the atoms near the surface, including the compression of top layer Al atoms towards the topmost oxygen layer (smallest arrow), the fusion of two Al layers below the topmost oxygen layer (middle arrow), and two distinct Al layers below the second oxygen layer (largest arrow). (c) Density profile of the MgO (004) surface. The layers are composed of alternating Mg and O atoms in lateral and vertical directions (red highlight). No surface reconstruction was observed. (d) Side view of the MgO (004) surface, which matches the density profile in (c) and shows no significant surface deformation. (e)

Density profile of the β -Ni(OH)₂ (0002) surface. No surface reconstruction was observed. Single peaks are observed for surface hydrogen, oxygen, and Ni atoms while the hydrogen peaks for the inner layers show two peaks from adjacent Ni(OH)₂ layers (red highlights). (f) Side view of the β -Ni(OH)₂ (0002) surface, which matches the density profile in (e) and shows no significant surface deformation.

2.9. Surface Modification in Aqueous Solution. As earlier shown for silica, phosphate, and aluminate surfaces, $^{30, 31, 42, 68}$ oxide surfaces in aqueous solution typically undergo hydration reactions, for example, $M_2O_3 + H_2O \rightarrow 2$ MO(OH), or $M_2O_3 + 3$ $H_2O \rightarrow 2$ M(OH)₃. The resulting superficial OH groups may be partly protonated, neutral, or deprotonated depending on the pH value in solution. Superficial hydration reactions from oxide to hydroxide, when equilibrium structures are considered, usually affect at least the surface atomic layer, and could proceed several atomic layers further into the bulk structure, especially under dissolution conditions at particularly low or high pH values. Consideration of these details is critical for *any* realistic simulation of electrolyte interfaces of oxides and their drastically changing properties as a function of pH value in solution.

A detailed discussion of surface chemistry and the data to quantitatively inform surface models will be shared in a follow-up contribution. Here, as an example, we consider alumina-type minerals (Al₂O₃), which feature characteristic AlO(OH) or Al(OH)₃ termination upon hydration. Correct modeling of these surfaces in aqueous electrolytes requires electroneutral Al₂O₃ models and at least one atomic layer of AlO(OH) or Al(OH)₃ termination when the pH value in solution is near ~8.4 (the point of zero charge as known from experiments). Under more acidic solution conditions between pH 8 towards 3, the AlO(OH) surface layers include an increasing

small percentage of AlO(OH₂)⁺ Cl⁻ surface groups. Under more alkaline conditions from pH 9 towards 13, AlO(OH) surface layers include an increasing small percentage of negatively charged AlO₂⁻ Na⁺ surface groups. To implement specific percentages of ionized groups as a function of pH value, we have previously used experimental reference data from surface titration. ¹⁴¹⁻¹⁴³ For alumina, the percentage of ionized AlO(OH) groups is 0% at pH ~ 8.4 and increases to ~10% AlO(OH₂)⁺ Cl⁻ groups at pH values of 3, as well as to ~10% AlO₂⁻ Na⁺ groups at pH values of 13, respectively. The atomic charges of H atoms and O atoms in OH groups in AlO(OH) and Al(OH)₃ are +0.25e and -0.79e, respectively. Typical bond and angle parameters for these surface groups can be taken from existing parameters in IFF. It is critical to obey charge neutrality upon ionization of AlO(OH) to AlO(OH₂)⁺ Cl⁻ and AlO₂⁻ Na⁺. No other dedicated or additional force field parameters are needed. LJ parameters for Al and O in the surface groups can be kept the same as in the bulk or used with minor modifications (see previous examples of silica³⁰ and hydroxyapatite³¹).

Using such chemically informed surface models makes a large difference in the affinity to counterions and charged organic molecules such as carboxylates, ammonium surfactants, and chelates to the oxide and hydroxide surfaces.^{30, 31} Meaningful force field parameters for the core compounds, as well as adequate surface models make the difference between reliable and unreliable simulations in equal parts.

2.10. Nonbonded Model for Silica, SiO₂. Silica is a key ingredient in glasses, nanoparticles, ceramics, and composites. The standard IFF model for silica is bonded, due to predominantly covalent bonding with atomic charges of Si of +1.1e versus a formal charge of +4e, and includes models for the full range of surface chemistry.^{26,30} Nonbonded silica models are therefore expected to be less accurate. Nevertheless, due to the absence of bond constraints, a set of nonbonded

parameters for silica can be useful for the simulation of mixed oxides, glasses, and ceramics, including amorphous melts prepared at high temperatures. Using our workflow and extensive tests (Figure 2d), we derived nonbonded models for silica in IFF-CVFF, OPLS-AA format as well as in IFF-CHARMM, AMBER formats that perform best in the nonbonded approximation (Table S4 in the Supporting Information). The atomic charges are +1.3e on the Si atoms and -0.65e on O atoms. 12-6 LJ parameters are $r_{min} = 1.6$ Å and $\epsilon = 0.15$ kcal/mol for silicon, as well as $r_{min} = 3.3$ Å and $\epsilon = 0.03$ kcal/mol for oxygen in IFF-CVFF, OPLS format. The values of r_{min} decrease slightly in IFF-CHARMM, AMBER format to 1.47 Å and 3.17 Å, respectively, since arithmetic combination rules result in longer Si-O bond lengths than geometric combination rules (Table S4 in the Supporting Information).

The performance of the nonbonded silica models is surprisingly good. The parameters reproduce the correct coordination numbers of 4 and 2, different crystal geometries and lattice parameters of α -quartz and α -cristobalite, as well as accurate surface energies (Table S5 in the Supporting Information). Bond lengths have ~3.5 % deviation and bond angles ~2% deviation from X-ray data. The density of α -quartz of 2.66 g/cm³ is reproduced within 0.5% deviation from X-ray data and the density of α -cristobalite of 2.33 g/cm³ is computed -4.5% lower with both types of IFF models (IFF-CVFF, OPLS and IFF-CHARMM, AMBER). The individual lattice parameters of α -quartz have deviations between $\pm 0.5\%$ and $\pm 0.7\%$. The (0001) resp. (001) surface energies of the two silica phases are $0.40 \pm 0.04 \text{ J/m}^2$ at 298 K according to measurements 144 , 145 and very well reproduced. The computed values are 0.44 J/m^2 for IFF-CVFF, OLPS and 0.40 J/m² for IFF-CHARMM, AMBER for quartz, and similar values for cristobalite. The bulk modulus of α -quartz was computed as 45 GPa with IFF-CVFF, OLPS and 44 GPa with IFF-CHARMM, AMBER, which is within the range of known measurements (35-45 GPa, 36.5 GPa often

reported). ^{30, 67, 146} The computed bulk modulus for α-cristobalite is, however, much too high at 44 GPa (expt: 11-17 GPa). ^{30, 67, 146} Accordingly, structural properties are in very good agreement with experimental data, and surface energies are excellent. Elastic constants and mechanical properties can have large deviations, and more details of the electronic structure would be required in the force field for better results. Overall, the nonbonded parameters for silica do not reach IFF level in terms of accuracy and transferability, however, they outperform existing nonbonded models in simplicity, speed, surface properties, and have a good level of compatibility.

The nonbonded silica model can be used to generate and equilibrate amorphous melts of silica and complex mixed glasses using annealing techniques, molecular dynamics simulation at high temperature, and cooling. Equilibrated models of such melts can be subsequently subjected to energy minimization and converted into the bonded IFF silica model, for local domains containing silica, for further analysis (every Si atom remains coordinated by 4 O atoms).^{26, 30}

2.11. Deployment of Oxide and Hydroxide Models. Simulation-ready structures and force field files are provided in the Supporting Information (Supporting Files), can be downloaded from the IFF website, and are available in the *Nanomaterial Modeler* module in CHARMM-GUI. The parameters can also be manually added to other force fields (AMBER, CHARMM, CFF, COMPASS, CVFF, DREIDING, GROMOS, OPLS-AA, PCFF, etc) into the correct sections. Simulation-ready models can be built under consideration of the masses, atomic charges, and force field types (Tables 2, 3, and Table S4 in the Supporting Information) using suitable software, e.g., Materials Studio, VMD, text editors, LAMMPS tools, GROMACS tools, or AMBER tools.

Using the IFF parameters and models of oxide and hydroxide nanostructures, the *Nanomaterial Modeler* module in CHARMM-GUI allows researchers to build interfaces of the oxides and hydroxides and the generation of simulation inputs in various file formats.⁵⁸ Figure 6 shows the

user interface of *Nanomaterial Modeler* for building models of metal oxides and hydroxides with a size of $30 \times 30 \times 30$ Å³. Hereby, the input dimension and the final model dimension can be different because of the unit cell size, and an estimated system size is displayed from the unit cell information (Figure 7a). *Nanomaterial Modeler* provides all-atom simulation inputs for various MD programs, including NAMD, ¹⁴⁷ GROMACS, ⁴⁴ AMBER, ¹⁴⁸ OpenMM, ¹⁴⁹ CHARMM, ¹⁵⁰ GENESIS, ¹⁵¹ and LAMMPS¹⁵², enabling researchers to employ any package of their choice (Figure 7b). To cover different cutoff methods used in various force field forms, the most widely used LJ treatments, such as 1) simple truncation at r = 12 Å (12 cutoff), standard in IFF, 2) forcebased switching over 10 to 12 Å (10-12 fsw), and 3) LJ particle mesh Ewald (LJPME), are supported in the input generation step. Details of the model building algorithm and input generation can be found in our previous report. ⁵⁸

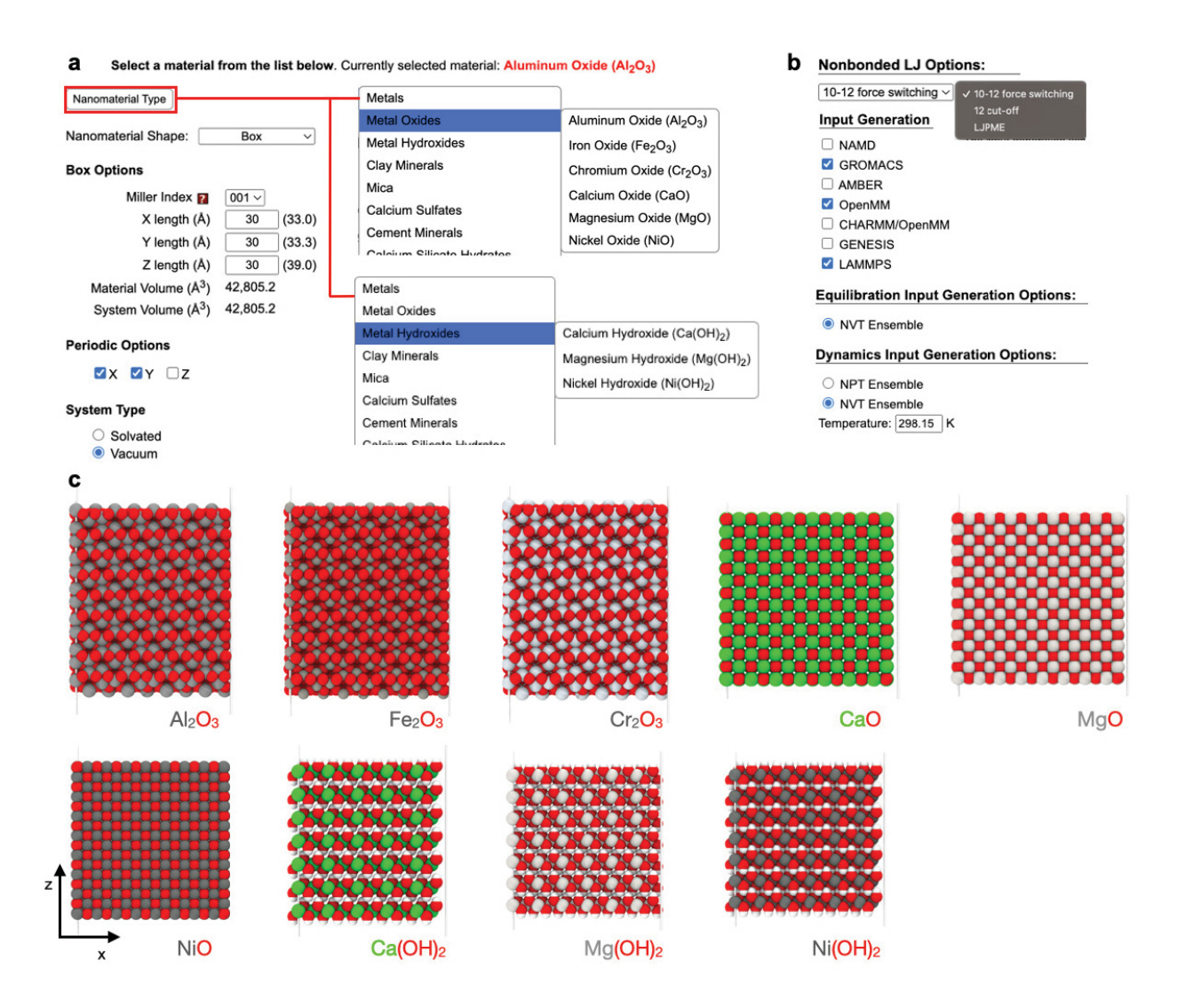


Figure 7. Model building with CHARMM-GUI *Nanomaterial Modeler*. (a) The user interface to select one of the available oxides and hydroxides. One can adjust the system size with X, Y and Z length options under "Box options". "Periodic Options" provides a method to define the periodicity of the system along each axis. (b) Available options for generating input files of various simulation programs. Three widely used LJ cutoff methods (i.e., simple truncation at r = 12 Å, force-based switching over 10 to 12 Å, and LJ particle mesh Ewald with no cutoff) are supported. (c) Examples of different surface models along the *z*-direction for the supported oxides and hydroxides.

The nonbonded character of the models further enables the analysis of complex mixed oxides, glasses, and certain chemical reactions. LJ and similar potentials have been previously used to model chemical reactions such as glass-forming reactions, the stability of mixed oxides (refs. 45, ¹⁵³ and our example of spinel above), hydration vs. dehydration reactions of salts, ⁴² and atom abstraction energies in catalysis. 154-156 Defect energies and vacancy transport can also be considered part of chemical reactions during oxidation and corrosion (refs. 157-160 and example of ion migration barriers above). The limitations for chemical reactions are significant, however. For example, multi-step reactions or complex chemical transformations are not feasible without additional assumptions. The main advantage of the models to approximate several reactions lies in the interpretability of the atomic charges and LJ parameters and the possibility to adjust to new chemical environments with limited effort. In addition, the prediction of structures and energy differences is more reliable than using DFT or other force fields (Table 1). Combinations of MD with QM methods can be explored at a local scale when electronic structure effects need to be included. The parameters or simulation protocols may be customized to represent a given chemical reaction, given experimental data and/or mechanistic knowledge, including realistic temperature, dynamics, and length scales.

2.12. Sensitivity of Force Field Parameters. The force field parameters for molecular simulations of oxide-based materials, organic, and biomolecular interfaces introduced here explore the limits of simple deterministic energy expressions. A comparison of the computed key properties using the different IFF flavors (Tables 4 to 7) and the magnitude of changes in parameters (Table 2) indicate the reliability and limitations. The sensitivity of computed properties to changes in force field parameters for a fixed energy expression is comparatively low, as further

illustrated in the methods section and in the Supporting Information (Tables S6 to S12). Uncertainties can also be assessed through the sensitivity of the nonbonded parameters to the combination rules when using 12-6 LJ potentials, as well as through the interplay of atomic charges with 9-6 LJ parameters when using the IFF-PCFF versus IFF-PCFF-HQ options. For example, exchanging the nonbonded parameters of IFF-CVFF, OPLS and IFF-CHARMM, AMBER would increase deviations in lattice parameters from ~0.2% up to several %, deviations in surface energies from ~7% up to ~15%, and deviations in bulk moduli from ~6% up to ~25%. This exchange of parameters is, however, not suggested and only demonstrates the impact of combination rules in nonbonded models.

2.13. Relationship to DFT/ML Trained Force Fields and Emerging Opportunities. DFT has had a profound impact in materials design and will continue to drive many exciting computational research areas. ^{57, 161} At the same time, we find much better reliability of IFF compared to DFT across the board, including the computed densities (<0.3% vs. 4% error), surface properties (8% vs. 25%, sometimes up to 50%), and bulk modulus (6% vs. 15%) (Table 1, Table 6, Table S2, and Section S4 in the Supporting Information). Similar improvements can be expected for computed defect energies and adsorption energies at interfaces. ¹³⁵ Therefore, using training data from IFF molecular dynamics simulations for machine learned (ML) potentials will lead to several times higher reliability than using training data from ab-initio MD simulations. ¹⁶²⁻¹⁶⁴ The differences will be particularly significant when considering a wider set of properties such as structures, energy differences, elastic properties, adsorption, electrolyte interfaces, organic and biological interfaces that are critical to design real materials and devices.

The computational speed of DFT/ML models also tends to be orders of magnitude slower than IFF MD, and usage for multiphase materials outside the training range is difficult. 165-167 For

example, IFF can be applied to aqueous and organic interfaces without additional parameter adjustments or training simulations. DFT/ML methods require further training calculations for every added chemical feature such as a different composition or type of adsorbed molecule, and the training calculations require about 10⁶ times more computational time compared to IFF MD simulations for the same system size. The practical value of DFT/ML-derived force fields and MD simulations for materials design is therefore somewhat unclear. The main benefit is the applicability to electronic structure problems, chemical reactions, and the expansion of ab-initio MD methos at the same level of limited reliability to a larger scale. Near-term applications likely include the same types of systems currently studied by DFT, such as mixtures of atoms and small molecules and discovery of new chemistries with limited complexity. Training ML-driven force fields with higher-level quantum methods (CCSD(T)) is desirable to increase the accuracy, however, the extreme computational demand reduces training systems to small sizes in vacuum (<100 atoms) that do not scale for applications such as solid-electrolyte interfaces, disordered, defective, or polymeric materials. A potential bottleneck is also the large pool of QM options and low interpretability of ML-generated potentials. In contrast, the small number of interpretable and well-performing parameters in IFF can serve as a reliable "chemical" code to speed up ML algorithms and accelerate materials design.

The proposition of "accurate" global machine learning force fields, so-called "modern machine learning force fields (MLFFs)"¹⁶⁴ therefore so far remains a myth. This work and earlier studies^{26-37, 57, 135, 168, 169} demonstrate that IFF performs several times better. MLFFs lack systematic benchmarks in virtually any domain including inorganic compounds as demonstrated here as well as biomolecular systems, e.g., DNA and proteins in solution, in comparison to biomolecular force fields. It is difficult to envision MLFFs in useful accuracy and interpretability anytime soon. More

AI, in combination with quantum methods, and developing AI tools to accelerate MD simulations with IFF and biomolecular FFs is likely to yield better results and faster progress in chemistry and materials science than attempting full scale ups with DFT/ML methods.

The reliability and speed of IFF MD in combination with CHARMM, AMBER, OPLS-AA, and PCFF/COMPASS creates opportunities for large-scale screening and training fast ML models for property predictions of inorganic, electrolyte, and biomolecular bulk systems and interfaces. Leading accuracy, fast training, and production speed could be sufficient for integration into autonomous laboratories to help answer experimental questions in real time.

3. Conclusion

This work introduces the to-date most accurate, efficient, and transferable force fields to simulate nine oxides, hydroxides, as well as their interfaces with solvents and organic molecules, and extends the INTERFACE force field for valuable chemistry space. The models employ primarily nonbonded parameters to represent Coulomb interactions and van-der-Waals interactions, including options for 12-6 and 9-6 Lennard-Jones (LJ) potentials. Primary validation involves (1) structural properties, represented by lattice parameters with <0.2% average deviation from X-ray data, (2) energy differences, represented by <10% average deviation in cleavage energies relative to experimental data, and (3) derivatives of energy differences, represented by <6% average deviation in bulk moduli from experimental data. The performance is, on average, several times to one hundred times higher than that of earlier force fields and DFT calculations. The workflow of derivation, interpretation, and validation can be applied to other compounds, expanding to a wider

chemistry space. We demonstrate prediction of the structure of mixed oxides, free energy barriers of ion transport through bulk oxides, as well as adsorption of water and organic molecules as a function of surface coverage in excellent agreement with experimental data. We also explain the origin and magnitude of surface reconstruction and introduce conceptually important surface models with pH-specific surface chemistry. Nonbonded silica models are introduced to support the simulation of glasses and multi-phase ceramics.

From a theory perspective, we achieve large improvements over prior methods by careful analysis of chemical bonding and atomic charges using standard IFF protocols, clear interpretation of Lennard-Jones (LJ) parameters, and in-depth validation using a comprehensive survey of state-of-the-art experimental data. Atomic charges follow consistent trends across the periodic table including atomization energies, electron affinities, and ionization energies. Missing covalent contributions in the nonbonded models are compensated by increased atomic charges and increased LJ well depths. The survey of experimental reference data often included more than 10 different sources for each data point and only a deep dive analysis of differences in laboratory methods, associated errors, chemical theory, viewpoints from DFT and other types of atomistic calculations allowed us to compile reliable reference data for surface energies and bulk moduli. The scarcity of reliable experimental data and 1:1 use in the appropriate context in simulations continues to be a major challenge, especially for conceptually critical surface energies.

We also witness the high scatter in DFT data in all key properties for validation and illustrate that DFT data alone are not suitable for benchmarking of physical properties, interatomic potentials, or molecular simulations of oxide and organic hybrid materials. DFT methods can contribute in a supportive way to add context to reproducible experimental data, offer qualitative guidance in case of sparse experimental data, or provide inspiration about electronic structure

effects. As a result, machine-learned potentials and MD simulations from DFT training data have between 3 times and 10 times lower accuracy than IFF MD, lower speed, and issues with transferability. The force field parameters and approaches for molecular simulations of oxide-based materials introduced in this work are suitable for mixtures of compounds included in IFF and in other organic and biomolecular force fields (CHARMM, AMBER, OPLS-AA, GROMOS, PCFF, COMPASS). A wide variety of oxide and hydroxide materials for catalysis, glasses, semiconductors, corrosion, ceramics, biomedical imaging, drug delivery, and functional polymer composites can be explored.

4. Computational Details

4.1. Development and Testing of Force Field Parameters. The reference state for validation of all oxide and hydroxide parameters was room temperature (298.15 K) and a pressure of 1 atm. The parameters can be applied to a wide range of temperatures and pressures without adjustments. The derivation of oxide models required 6 nonbond parameters, which include the atomic charge (q) and LJ parameters (r_{min} and ε) for metal and oxygen. Atomic charges were assigned based on available experimental data and with the help of extended-Born cycle relative to already known chemically similar compounds from experimental data and in IFF. Charges of metal and oxygen atoms are linked to the stoichiometry of the oxide to maintain charge neutrality. The values were iteratively increased to account for covalent bonding contributions, which have no explicit representation in the nonbonded model (typically no more than +20%). The atomic diameter, r_{min} , was adjusted to match the atomic positions and the density of the compounds. Epsilon was adjusted to match the surface energy. Lastly, all the parameters were refined iteratively to match density and lattice parameters within 0.5%, surface energy within 5%, and bulk modulus within 10% of

the experimental value, which are the typical IFF targets (Figure 2d). The models of hydroxides required an additional equilibrium bond distance (r_0) and bond stretching constant (K_b) for OH bonds, as well as LJ parameters for the hydrogen atom. The value of r_0 was obtained from the crystal structure of the hydroxide and K_b by tuning the computed IR/Raman spectrum of the OH bond in the hydroxide to experimental data. LJ parameters for hydrogen are zero (negligible) in the 12-6 LJ form and small for the 9-6 LJ potential, equal to the parameters in the corresponding flexible SPC water models and other hydroxide compounds in IFF.

4.2. Sensitivity of Computed Properties to the Chosen Energy Expression and Force Field Parameters. We offer four types of IFF models for each core compound including two LJ functional forms. IFF-CVFF, OLPS and IFF-CHARMM, AMBER models use the 12-6 form of the LJ potential with geometric or arithmetic mixing rules for r_{min} , respectively (Figure 4c). Differences in the mixing rules for the 12-6 LJ parameters between different atom types typically require rebalancing of nonbonded parameters (atomic charge, r_{min} , and epsilon) to best reproduce the experimental density, surface energy, and bulk modulus, depending upon the crystal structure (Table 2). IFF-PCFF and IFF-PCFF-HQ models use the 9-6 form of the LJ potential. PCFF uses the same atomic charges as in the 12-6 LJ varieties and IFF-PCFF-HQ uses somewhat higher atomic chargesnecessary to match the bulk modulus. The performance of the (IFF-CVFF, OLPS), (IFF-CHARMM, AMBER), and IFF-PCFF-HQ models is equivalent, while IFF-PCFF models match the density, the surface energy, and yield a bulk modulus that is \sim 20% too low.

The sensitivity of computed properties to changes in nonbond parameters for the same energy expression, including the same combination rules, is low (Tables S6 to S11 in the Supporting Information). When modified parameters continue to reproduce lattice parameters, often equally consistent models can be obtained with changes in atomic charges up to 5% and in LJ parameters

up to 10%. The sensitivity of the computed binding energy of organic molecules on the mineral surfaces as a function of the chosen nonbond parameters is low (Table S12 in the Supporting Information). The values of the binding energies change only by about 5% for different sets of nonbond parameters, which include changes in atomic charges and in LJ parameters up to 10%, under the condition that the lattice parameters (and surface energy) remain approximately the same. The relatively low and manageable sensitivity can be helpful for AI-supported learning of IFF potentials for new chemistries.

4.3. Density and Lattice Parameters. To compute the density and lattice parameters, models of the unit cells of the oxides and hydroxides from X-ray data (Figure 1b) were repeated in space to create a 3D periodic box of ~1.9 x 1.9 x 1.9 nm³, or larger, to reduce interactions with periodic images to a negligible level. The structures were subjected to MD simulations in the NPT ensemble at 298.15 K and 1 atm pressure using the Discover program in Materials Studio. 170 Velocity scaling with a temperature window of 10 K was used as a thermostat, and the Parinello-Raman method was used as a barostat, which allows accurate responses to changes in pressure. The total simulation time was at least 250 ps (no changes after ~50 ps), and we employed a 0.5 fs time-step to lower fluctuations in instantaneous stress (helpful during validation and usually not needed for applications of the model). The system was equilibrated during an initial block of 100 ps and data was collected for the latter block of 150 ps. The calculation of equilibrium lattice parameters and the density in high accuracy required only short simulations of 250 ps, and average values were reported for the last block of 150 ps in equilibrium. We also tested that equilibrium lattice parameters did not change after several nanoseconds, and even hundreds of nanoseconds of MD simulation within the statistical uncertainty of <0.1%. The cutoff for van-der-Waals pairwise

interactions using Lennard-Jones parameters was set at 12 Å, equal to the IFF convention. Coulomb interactions were calculated using Ewald summation with high accuracy of 10⁻⁵.

The target for validation was to achieve a deviation of no more than 1 % in density and <0.5% in lattice parameters (all cell constants and angles) relative to experimental reference data and achieved in most cases. The lattice parameters were also independently tested by 200 to 500 steps geometry optimization. These calculations are complete very fast within seconds and correspond to data at 0 K temperature. The lattice parameters from energy minimization were a fraction of a percent smaller than at 298 K due to thermal contraction.

4.4. Surface Energy. The first step in the calculation of the surface energy, or cleavage energy, is the choice of the (hkl) surface (Figure 8). Out of the unlimited number of theoretically possible (hkl) cleavage planes, the cleavage plane of minimum energy usually accounts for a large part of the exposed crystal surface in equilibrium and can often be selectively analyzed in experiments using crack propagation experiments (Figure 1b and dashed lines in Figure 8). The cleavage planes of lowest energy are (0001) for the corundum-type structures, (004) for the rock-salt type crystal structures, and (0002) for the hydroxides. Some cleavage planes of lowest energy, namely, (004) for MO and (0002) for M(OH)₂, have sometimes been inaccurately reported as (001) and (0001) planes, likely due to limitations in atomic-level characterization tools. According to our calculations, cleavage of the actual (001) and (0001) planes would lead to surfaces of much higher energy and immediate surface reconstruction.

To calculate the surface energy, models for the bulk mineral and for two cleaved surfaces were created (Figure 8). The surface models contained the same number of atoms as the bulk system and have identical box dimensions. The lattice parameters for the bulk model in the lateral directions upon cleavage were hereby equal to equilibrium values obtained from prior simulations

in the NPT ensemble. The bulk system comprised a thick slab of \sim 2 x 2 x 4 nm³ size in contact with a vacuum slab of \sim 10 nm thickness (labeled "Bulk" in Figure 8a-c). The surface system was composed of two thin slabs of dimension \sim 2 x 2 x 2 nm³, which were created by moving the atoms atop the cleavage plane by \sim 5 nm away from the atoms below the cleavage plane, leaving sufficient vacuum space in between (labeled "Surf" in Figure 8a-c). This procedure cleaves the original bulk slab and generates two new surfaces, and has been routinely used for the validation of surface energies of solids in IFF. $^{27, 112}$ Metal cations along the (0001) cleavage plane for corundum-type oxides, as well as hydroxide ions along the (0002) cleavage plane for metal hydroxides were then divided equally between the two newly created surfaces to ensure local and global charge neutrality, as well as zero net dipole moment of the created surface slabs (Figure 8a, c). The lowest energy cleavage plane (004) of the metal oxides of MO type, which have the rock salt (NaCl) structure, falls between atomic layers which are locally charge-neutral by themselves and were separated to create the surfaces (Figure 8b).

Subsequently, the bulk and the surface system were subjected to molecular dynamics simulation in the NVT ensemble using the Discover program. The settings for molecular dynamics simulations were the same (time step, thermostat, cutoffs) as for the computation of lattice parameters in the NPT ensemble, except for not needing a barostat. First, a short MD simulation was run for 100 ps at an elevated temperature of 573 K to mildly anneal both the bulk and surface models. This protocol enhances configuration sampling to capture surface reconstruction upon cleavage. Annealing accelerates rearrangements of the atoms at the surface, if thermodynamically preferred, at low computational cost, as a proxy towards capturing time scales closer to experiments. Second, the two systems were subjected to molecular dynamics simulation at 298.15 K for 250 ps and the average total equilibrium energy of the two systems was recorded over the

last 150 ps. Third, the surface energy was calculated as a difference in the total energy between the two systems (bulk and surface), and divided by the total area of the two newly generated surfaces (2A): 26,31,35,60,84,85,112

Surface energy,
$$E_S = \frac{E_{Surf} - E_{Bulk}}{2A}$$
. (1)

The values are reported in J/m^2 and have a statistical uncertainty of $\pm 1\%$.

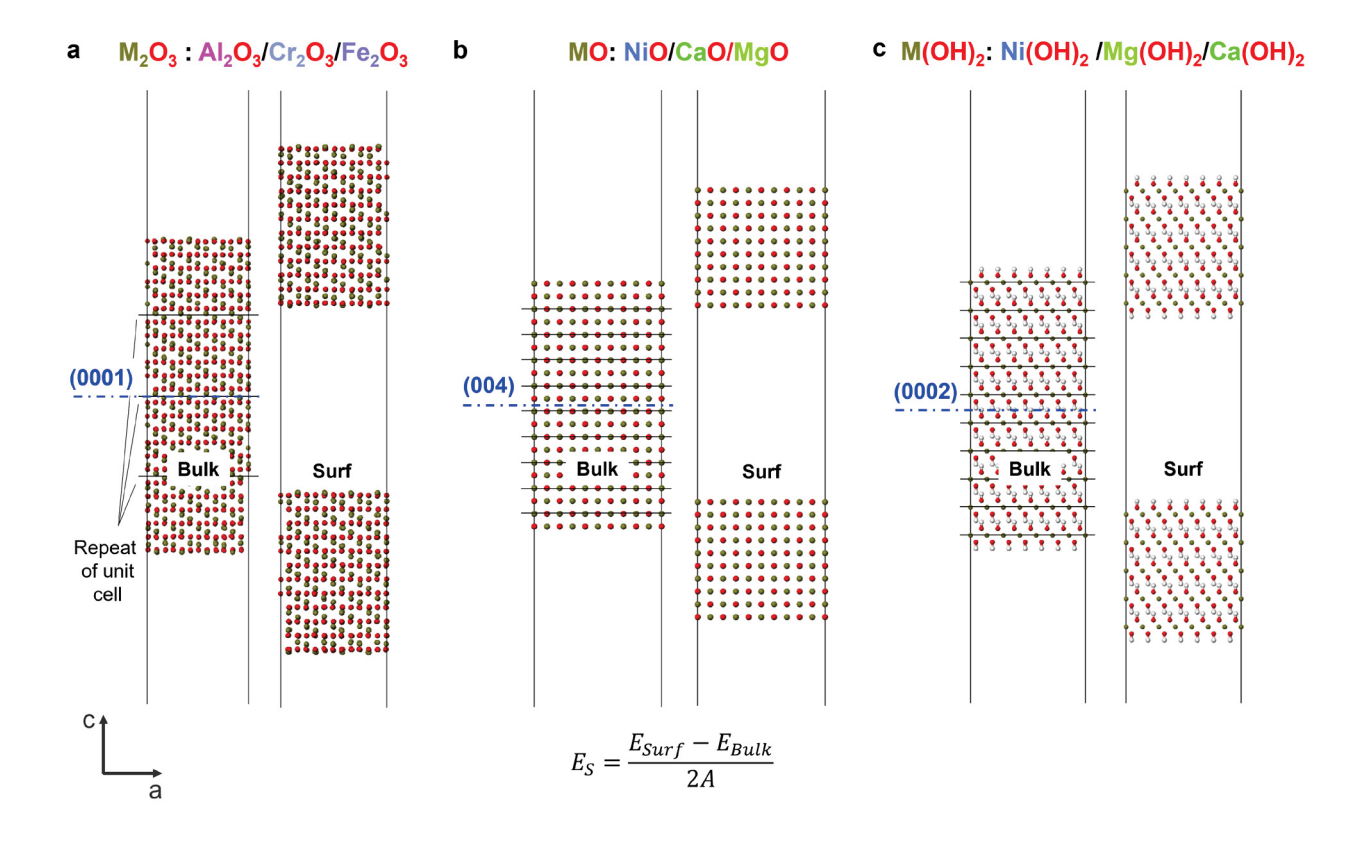


Figure 8. Identification of the (hkl) cleavage planes of lowest energy and the simulation protocol for the calculation of the surface energy E_S (in J/m²). (a) Bulk structure of M₂O₃ and the (0001) cleavage plane. (b) Bulk structure of MO and the (004) cleavage plane. (c) Bulk structure of M(OH)₂ and the (0002) cleavage plane. Repeat units of the unit cells along the c axis are indicated. First, cleavage planes were defined (blue dashed lines). Second, surfaces were created by moving

the two slabs on either side of the cleavage plane apart (~5 nm). Here, consideration of charge neutrality for each surface and creating no, or minimal local dipole moments are critical to repreent equilibrium cleavage. For example, atomic layers of charged Al³⁺ ions in (a) were 50/50 distributed on each the two created surfaces in a statistical manner to minimize internal electric fields. Third, mild annealing and surface relaxation were carried out to redistribute ions and allow for equilibrium surface reconstruction, which was especially important for surfaces of M(OH)₂ and M₂O₃ post cleavage.

4.5. Bulk Modulus. A 3D periodic box of at least ~2 x 2 x 2 nm³ size was created from the unit cells of the oxides and hydroxides (Figure 1). The simulation protocol to calculate the bulk modulus involved molecular dynamics in the NPT ensemble and was equal to that of the calculation of lattice parameters and density. The simulations were then run at two additional pressures for 250 ps to observe change in volume. Typically, we considered pressures between 0.2 GPa and 0.5 GPa, equal to somewhat less than 1% strain within the linear regime of stress vs strain curve. Upon changing the pressure from 0.2 to 0.5 GPa, the average standard deviation in computed bulk modulus was observed to be ± 2 GPa. The bulk modulus was calculated from the difference in average pressure P_f relative to 1 atm ($P_0 = 1$ atm) and the difference in average volume relative to the volume at 1 atm pressure (V_0):

Bulk Modulus,
$$K = -V_0 \frac{(P_f - P_0)}{(V_f - V_0)}$$
 (2)

The average pressure and volume were recorded during the equilibrium part of the trajectory (last 150 ps). The overall average standard deviation in computed bulk modulus was ± 4 GPa.

4.6. Simulation Protocols Using Pedone, CLAYFF, ReaxFF, and UFF Potentials. Data for the Pedone potential were inferred from the original references. We attempted an implementation

of the Pedone potential in LAMMPS (Section S1 and files in the Supporting Information). Simulations with the Pedone potential proved to be challenging and surface or interfacial properties are not accessible. The simulations with CLAYFF were run using the same protocols as for IFF using the NAMD program, including Ewald summation for Coulomb interactions in high accuracy, a 12 Å cutoff for LJ interactions, and typical simulation times of 250 ps. ^{51,52} Differences to using a cutoff of 8 Å were found to be small. ReaxFF simulations were carried out using the program LAMMPS and the "pair_style reax/c" command for 500 ps, along with recommended simulation settings. Sample files to repeat the calculations with CLAYFF and ReaxFF are provided as part of supporting files. Calculations with UFF were carried out in Materials Studio using automated atom types and charges, and otherwise the same simulation protocols as for IFF.

- **4.7. Analysis of the Properties of Spinel.** The model of MgAl₂O₄ was built using X-ray data from the ACSD and had a size of 2.427 x 2.427 nm³. The simulation protocols to analyze the lattice parameters, density, and bulk modulus were as reported above.
- **4.8. Cation Migration.** Cation migration was analyzed using steered molecular dynamics to monitor free energy barriers. We used large models of cubic oxide crystals of approximately 8.0 x 8.0 x 8.0 nm³ size (Figure S1 in the Supporting Information). First, the lattice was equilibrated by MD simulation in the NPT ensemble within the range of experimental temperature. For CaO, the measurement temperature was between 1000 to 1400 °C and a temperature of 1473 K (1200 °C) was chosen in the simulation. Teo NiO, the measurement temperature was between 500 and 800 °C and a temperature of 923 K (650 °C) was chosen in the simulation. A Schottky defect, consisting of a cation vacancy and an anion vacancy, maintaining electroneutrality, was created in the model. We used a large separation, i.e., a cation vacancy at the center of the model and an anion vacancy near the vertex of the equilibrated crystal to obtain cation migration barriers that are not

influenced by the location of the anion. Steered molecular dynamics simulations were performed to pull the metal cation nearest to the cation vacancy at the center of the crystal from the layer below the row of atoms that contains the cation vacancy in the direction of the z-axis into the existing vacancy (Figure 3f and Figure S1 in the Supporting Information). The cation migrated at a rate of 1 Å/ns. All other atoms were mobile except the atoms along the y-axis between 0 to 3.5 Å, which avoided unwanted crystal deformation due to applied external velocity and resulting force (Figure S1, yellow region, in the Supporting Information). The input files and crystal structures used to run the simulation in LAMMPS are provided as part of the Supporting Information.

4.9. Adsorption Energy of Water and Alkanes on MgO Surfaces. The adsorption energy of water molecules on the MgO (004) surface was computed in a periodic box containing an MgO slab of 21.055 x 21.055 x 21.055 Å³ size with a vacuum slab of 250 Å length along z-axis using the program LAMMPS. To obtain the binding energy at 0 K, a water molecule was placed in different upright and flat configurations near the surface of MgO, molecular mechanics with the conjugate gradient algorithm was used to minimize the energy and to identify the structure of lowest energy (Figure 4a, b). Then, the energy by placing the water molecule 125 Å away from the MgO (004) surface was obtained upon energy minimization. The difference in energy was computed between the two states to report the binding energy at 0 K (Figure 4a). To obtain the binding energy of a single water molecule at 170 K on the same surface, two molecular dynamics simulations were carried out, one with the water molecule near the surface, and another with the water molecule approximately 125 Å away from the surface using the NVT ensemble, a time step of 1 fs, and a total simulation time of 200 ps with the program LAMMPS. The average energies in equilibrium in the bound and detached states were calculated, and the difference is reported as

binding energy of water at 170 K (Figure 4b). Care was taken to compute the average total energy in the away state by using the equilibrated part of simulation when the water molecule is at least 30 Å away from the MgO (400) surface.

The binding energy of one monolayer of water molecules adsorbed on the MgO (400) surface was computed by subtracting the average total energy of water molecules in the gaseous state and of the MgO slab from the average total energy of the monolayer of water molecules adsorbed on the MgO (400) slab. The energy difference was divided by the total number of water molecules and reported per mol of water (Figure 4c). The average total energy of water molecules in the vapor phase was computed by placing 125 isolated water molecules in a 100 nm³ cubic box and running an MD simulation at 170 K with a timestep of 1 fs for 100 ps. In the initial configuration, each water molecule was at least 20 nm away from the nearest neighbor, and the average energy was computed from the equilibrium part of simulation when the molecules stayed at least 10 nm away from the nearest neighbor. Since 50 water molecules were adsorbed on the surface of the MgO 21.055 Å³ cubic slab at 1 ML configuration (Figure 4c), the energy of 125 water molecules was scaled to obtain the energy for 50 water molecules in the vapor phase. The average total energy of the MgO 21.055 Å³ cubic slab with 100 Å vacuum space along z-axis was computed by running an MD simulation in the NVT ensemble at 170 K for 150 ps and using the equilibrated part of the trajectory. Finally, the monolayer configuration of water molecules was obtained by initially placing 200 water molecules above the MgO (400) surface slab with 100 Å vacuum space along the z-axis and gradually lowering the temperature to 170 K in three steps, starting with 500 K, 350 K and 250 K, for annealing and sufficient configuration sampling. At each temperature step, MD simulations were run for 100 ps in the NVT ensemble. After the last run at 170 K, the water molecules present in second layer and beyond were deleted from the simulation box. Then, the

simulation was continued with only 1 monolayer of water molecules adsorbed on the surface for 200 ps at 170 K to obtain the average total equilibrium energy of 1 ML of water molecules bound to the MgO (400) surface.

Models of the alkanes C₂H₆, n-C₄H₁₀ and n-C₈H₁₈ adsorbed onto the MgO (100) surfaces (more precisely, (400) surfaces) of an area of ~6.1 x 6.1 nm² were obtained in two steps. First, approximately two monolayers of alkane molecules were placed on the (400) surface of MgO, visually covering the entire surface area. The structure was equilibrated for 0.5 ns using the NVT ensemble (Figure S2a, c, e in the Supporting Information). Second, the molecules forming the second layer in the equilibrated adsorbed configuration were selected and deleted to obtain an adsorbed configuration at monolayer coverage (Figure S2b, d, f in the Supporting Information). The monolayer structure was then further equilibrated for 0.5 ns (Figure 5a, c and e). To obtain an equilibrium structure at 0.5 ML surface coverage, half of the alkane molecules from the monolayer configuration (at 1.0 ML) were removed and the remaining structure was run for another 0.5 ns (Figure 5b, d and f). The total average energy of the MgO (400) surface slab (E_{MgO}) and of the alkane molecules (E_{alkane}) were calculated separately. To obtain the adsorption energy (Table 8), the total energy of the MgO surface slab and of the alkane molecules was subtracted from the energy of the system with alkane molecules adsorbed on the (400) MgO surface:

$$E_a = E_{Alkane+MgO} - \left(E_{MgO} + N_a \cdot E_{Alkane}\right) \tag{3}$$

Hereby, E_a is the cumulative adsorption energy at monolayer or half monolayer coverage, E_{MgO} is the energy of the MgO slab, E_{Alkane} is the energy of one alkane molecule and N_a is the total number of molecules adsorbed. All the simulations were run using the NAMD program, the IFF-CHARMM, AMBER parameters for the MgO surface, and available parameters for alkane molecules in the CHARMM36 force field. The simulations were run at 75 K, 111 K and 175 K for

 C_2H_6 , n- C_4H_{10} and n- C_8H_{18} systems respectively, matching the measurement temperatures of the respective TPD experiments. The results from eq. (3) were reported on a per-molecule basis, i.e., as a value of E_a/N_a , the adsorption energy per single molecule at 1.0 monolayer or 0.5 monolayer coverage, respectively (Table 8).

4.10. Model Uncertainties and Limitations. The models reproduce density, surface energy and bulk modulus of the oxides and hydroxides as close to experiments as possible, exploiting the limits of the IFF energy expressions and combination rules. We identified and analyzed cleavage planes of minimum energy for each crystal structure. Other (hkl) surfaces can be examined and, in case of less stable surfaces, bonded parameters may be added to constrain atoms at desired positions. In the assessment of mechanical properties, our focus on the reproduction of the bulk modulus may not be sufficient to reproduce all the elastic constants, which can be explored in further work. For simulations in aqueous environment, bare oxide surfaces often require modification to models of hydrated surfaces with a superficial layer of hydroxide (neutral, protonated, or deprotonated) as described in Section 2.9.¹⁴¹⁻¹⁴³ Uncertainties and potential errors are described in the respective sections.

Supporting Information Available: Supporting tables and supporting text showing a comparison of lattice parameters in experiment relative to IFF, other potentials, and DFT data in the OpenKIM database, computed surface energies using various earlier methods, a detailed survey of experimentally measured bulk moduli, the nonbonded IFF potential for silica, extensive data showing the dependence of computed properties with IFF on the choice of force field parameters; Supporting figures showing the protocol for carrying out simulations of cation migration and formation of alkane monolayers adsorbed on MgO (400) surfaces; Supporting text describing the

implementation of the Pedone potential in LAMMPS; Supporting files including simulation-ready models of crystal structures and force field files in IFF-CVFF, IFF-CHARMM, IFF-PCFF and IFF-PCFF-HQ formats for all oxides and hydroxides, files to reproduce the simulation of the spinel crystal structure, of cation migration in the oxides, and of hydrocarbon adsorption on oxide surfaces.

Acknowledgement: The authors acknowledge support by the National Science Foundation (OAC 1931587, CMMI 1940335), BASF, and the University of Colorado Boulder. We acknowledge helpful comments by Dr. Eduard Schreiner, BASF. We utilized allocations of computational resources at the Argonne Leadership Computing Facility, supported by the Office of Science of the U.S. Department of Energy (DE-AC02-06CH11357), and at the Summit supercomputer, a joint effort of the University of Colorado Boulder and Colorado State University supported by the National Science Foundation (ACI 1532235 and ACI 1532236).

References

- 1. Axinte, E., Glasses as Engineering Materials: A Review. *Mater. Des.* **2011**, *32*, 1717-1732.
- 2. Misra, R.; Misra, K. P., Fundamentals of Ceramics: Introduction, Classification, and Applications. In *Ceramic Science and Engineering*, Elsevier: 2022; pp 5-20.
- 3. Chakrabarty, S.; Chatterjee, K., Synthesis and Characterization of Nano-Dimensional Nickelous Oxide (NiO) Semiconductor. *J. Phys. Sci.* **2009**, *13*, 245-250.
- 4. Choong, C. K.; Chen, L.; Du, Y.; Schreyer, M.; Ong, S. D.; Poh, C. K.; Hong, L.; Borgna, A., The Role of Metal–Support Interaction for CO-Free Hydrogen From Low Temperature Ethanol Steam Reforming on Rh–Fe Catalysts. *Phys. Chem. Chem. Phys.* **2017**, *19*, 4199-4207.
- 5. de Toledo, L. d. A. S.; Rosseto, H. C.; Bruschi, M. L., Iron Oxide Magnetic Nanoparticles as Antimicrobials for Therapeutics. *Pharm. Dev. Technol.* **2018**, *23*, 316-323.
- 6. Mitchell, M. J.; Billingsley, M. M.; Haley, R. M.; Wechsler, M. E.; Peppas, N. A.; Langer, R., Engineering Precision Nanoparticles for Drug Delivery. *Nat. Rev. Drug Discovery* **2021**, *20*, 101-124.
- 7. Zhang, Z.; Gesmundo, F.; Hou, P.; Niu, Y., Criteria for The Formation of Protective Al_2O_3 Scales on Fe–Al and Fe–Cr–Al Alloys. *Corros. Sci.* **2006**, *48*, 741-765.

- 8. Mott, N., The Theory of the Formation of Protective Oxide Films on Metals.—III. *Trans. Faraday Soc.* **1947,** *43*, 429-434.
- 9. Nikita, K.; Henderson, J., Glass Analyses from Mycenaean Thebes and Elateia: Compositional Evidence for a Mycenaean Glass Industry. *J. Glass Stud.* **2006**, *48*, 71-120.
- 10. Wyckoff, R., *Crystal Structures , Second Edition New York, New York Rocksalt Structure.* Interscience Publishers: 1963; Vol. 1, p 85-237.
- 11. Hazen, R. M., Effects of Temperature and Pressure on the Cell Dimension and X-Ray Temperature Factors of Periclase. *Am. Mineral.* **1976**, *61*, 266-271.
- 12. Fiquet, G.; Richet, P.; Montagnac, G., High-Temperature Thermal Expansion of Lime, Periclase, Corundum and Spinel. *Phys. Chem. Miner.* **1999,** *27,* 103-111.
- 13. Henderson, D.; Gutowsky, H., A Nuclear Magnetic Resonance Determination of the Hydrogen Positions in Ca(OH)₂. *Am. Mineral.: J. Earth Planet. Mat.* **1962,** *47*, 1231-1251.
- 14. NEWNHAM, E.; DE HAAN, Y., Refinement of the a Al_2O_3 , Ti_2O_3 , V_2O_3 and Cr_2O_3 structures. *Z. Kristallogr. Cryst. Mater.* **1962**, *117*, 235-237.
- 15. Blake, R.; Hessevick, R.; Zoltai, T.; Finger, L. W., Refinement of the Hematite Structure. *Am. Mineral.*: *J. Earth Planet. Sci. Lett.* **1966**, *51*, 123-129.
- 16. Fukui, H.; Ohtaka, O.; Suzuki, T.; Funakoshi, K., Thermal Expansion of Mg(OH)₂ Brucite Under High Pressure and Pressure Dependence of Entropy. *Phys. Chem. Miner.* **2003**, *30*, 511-516.
- 17. Heinz, H.; Pramanik, C.; Heinz, O.; Ding, Y.; Mishra, R. K.; Marchon, D.; Flatt, R. J.; Estrela-Lopis, I.; Llop, J.; Moya, S.; Ziolo, R. F., Nanoparticle Decoration with Surfactants: Molecular Interactions, Assembly, and Applications. *Surf. Sci. Rep.* **2017**, *72*, 1-58.
- 18. King, A. D.; Birbilis, N.; Scully, J. R., Accurate Electrochemical Measurement of Magnesium Corrosion Rates; a Combined Impedance, Mass-Loss and Hydrogen Collection Study. *Electrochim. Acta* **2014**, *121*, 394-406.
- 19. Ramanathan, R.; Ramalingam, G.; Perepezko, J. H.; Reinke, P.; Voorhees, P. W., Evolution of NiO Island Size Distributions during the Oxidation of a Ni-5Cr Alloy: Experiment and Modeling. *ACS Appl. Mater. Interfaces* **2018**, *10*, 9136-9146.
- 20. Yang, Y.; Zhou, J. H.; Zhu, F.; Yuan, Y. K.; Chang, D. J.; Kim, D. S.; Pham, M.; Rana, A.; Tian, X. Z.; Yao, Y. G.; Osher, S. J.; Schmid, A. K.; Hu, L. B.; Ercius, P.; Miao, J. W., Determining the Three-Dimensional Atomic Structure of an Amorphous Solid. *Nature* **2021**, *592*, 60-64.
- 21. Xu, R.; Chen, C.-C.; Wu, L.; Scott, M. C.; Theis, W.; Ophus, C.; Bartels, M.; Yang, Y.; Ramezani-Dakhel, H.; Sawaya, M. R.; Heinz, H.; Marks, L. D.; Ercius, P.; Miao, J., Three-Dimensional Coordinates of Individual Atoms in Materials Revealed by Electron Tomography. *Nat. Mater.* **2015**, *14*, 1099-1103.
- 22. Zhou, J.; Yang, Y.; Kim, D. S.; Yuan, A.; Tian, X.; Ophus, C.; Sun, F.; Schmid, A. K.; Nathanson, M.; Heinz, H.; An, Q.; Zeng, H.; Ercius, P.; Miao, J., Observing Crystal Nucleation in Four Dimensions Using Atomic Electron Tomography. *Nature* **2019**, *570*, 500-503.
- 23. Dharmawardhana, C. C.; Zhou, J. H.; Taylor, M.; Miao, J. W.; Perepezko, J. H.; Heinz, H., Reactive Modeling of Mo3Si Oxidation and Resulting Silica Morphology. *Acta Mater.* **2020**, *187*, 93-102.
- 24. Prins, R., On the Structure of Gamma-Al2O3. J. Catal. 2020, 392, 336-346.
- 25. Heinz, H.; Ramezani-Dakhel, H., Simulations of Inorganic–Bioorganic Interfaces to Discover New Materials: Insights, Comparisons to Experiment, Challenges, and Opportunities. *Chem. Soc. Rev.* **2016**, *45*, 412-448.
- 26. Heinz, H.; Lin, T.-J.; Mishra, R. K.; Emami, F. S., Thermodynamically Consistent Force Fields for the Assembly of Inorganic, Organic, and Biological Nanostructures: The INTERFACE Force Field. *Langmuir* **2013**, *29*, 1754-1765.
- 27. Kanhaiya, K.; Kim, S.; Im, W.; Heinz, H., Accurate Simulation of Surfaces and Interfaces of Ten FCC Metals and Steel Using Lennard–Jones Potentials. *npj Comput. Mater.* **2021,** *7*, 17.

- 28. Hoff, S. E.; Di Silvio, D.; Ziolo, R. F.; Moya, S. E.; Heinz, H., Patterning of Self-Assembled Monolayers of Amphiphilic Multisegment Ligands on Nanoparticles and Design Parameters for Protein Interactions. *Acs Nano* **2022**, *16*, 8766-8783.
- 29. Emami, F. S.; Puddu, V.; Berry, R. J.; Varshney, V.; Patwardhan, S. V.; Perry, C. C.; Heinz, H., Prediction of Specific Biomolecule Adsorption on Silica Surfaces as a Function of pH and Particle Size. *Chem. Mater.* **2014**, *26*, 5725–5734.
- 30. Emami, F. S.; Puddu, V.; Berry, R. J.; Varshney, V.; Patwardhan, S. V.; Perry, C. C.; Heinz, H., Force Field and a Surface Model Database for Silica to Simulate Interfacial Properties in Atomic Resolution. *Chem. Mater.* **2014**, *26*, 2647-2658.
- 31. Lin, T. Z.; Heinz, H., Accurate Force Field Parameters and pH Resolved Surface Models for Hydroxyapatite to Understand Structure, Mechanics, Hydration, and Biological Interfaces. *J. Phys. Chem. C* **2016**, *120*, 4975-4992.
- 32. Heinz, H.; Vaia, R. A.; Krishnamoorti, R.; Farmer, B. L., Self-Assembly of Alkylammonium Chains on Montmorillonite: Effect of Chain Length, Head Group Structure, and Cation Exchange Capacity. *Chem. Mater.* **2007**, *19*, 59-68.
- 33. Javadi, A.; Jamil, T.; Soucek, M. D.; Heinz, H., Working Mechanisms and Design Principles of Comb-like Polycarboxylate Ether Superplasticizers in Cement Hydration: Quantitative Insights for a Series of Well-Defined Copolymers. *ACS Sustainable Chem. Eng.* **2021**, *9*, 8354-8371.
- 34. Jamil, T.; Javadi, A.; Heinz, H., Mechanism of Molecular Interaction of Acrylate-Polyethylene Glycol Acrylate Copolymers with Calcium Silicate Hydrate Surfaces. *Green Chem.* **2020**, *22*, 1577-1593.
- 35. Liu, J.; Zeng, J.; Zhu, C.; Miao, J.; Huang, Y.; Heinz, H., Interpretable Molecular Models for Molybdenum Disulfide and Insight into Selective Peptide Recognition. *Chem. Sci.* **2020**, *11*, 8708-8722.
- 36. Pramanik, C.; Gissinger, J. R.; Kumar, S.; Heinz, H., Carbon Nanotube Dispersion in Solvents and Polymer Solutions: Mechanisms, Assembly, and Preferences. *Acs Nano* **2017**, *11*, 12805-12816.
- 37. Kanhaiya, K.; Heinz, H., Adsorption and Diffusion of Oxygen on Pure and Partially Oxidized Metal Surfaces in Ultrahigh Resolution. *Nano Lett.* **2022**, *22*, 5392-5400.
- 38. Hill, R. J., Crystal-Structure Refinement and Electron-Density Distribution in Diaspore. *Phys. Chem. Miner.* **1979,** *5*, 179-200.
- 39. Belokoneva, E. L.; Shcherbakova, Y. K., Electron Density in Synthetic Escolaite Cr2O3 with a Corundum Structure and Its Relation to Antiferromagnetic Properties. *Russian J. Inorg. Chem.* **2003**, *48*, 861-869.
- 40. Lewis, J.; Schwarzenbach, D.; Flack, H. D., Electric Field Gradients and Charge Density in Corundum, α-Al2O3. *Acta Cryst. A* **1982**, *38*, 733-739.
- 41. Heinz, H.; Suter, U. W., Atomic Charges for Classical Simulations of Polar Systems. *J. Phys. Chem. B* **2004**, *108*, 18341-18352.
- 42. Mishra, R. K.; Kanhaiya, K.; Winetrout, J. J.; Flatt, R. J.; Heinz, H., Force Field for Calcium Sulfate Minerals to Predict Structural, Hydration, and Interfacial Properties. *Cem. Concr. Res.* **2021**, *139*, 106262.
- 43. Li, S.; Liu, J.; Ramesar, N. S.; Heinz, H.; Xu, L.; Xu, C.; Kotov, N. A., Single- and Multi-Component Chiral Supraparticles as Modular Enantioselective Catalysts. *Nat. Comm.* **2019**, *10*, 4826.
- 44. Abraham, M. J.; Murtola, T.; Schulz, R.; Páll, S.; Smith, J. C.; Hess, B.; Lindahl, E., GROMACS: High Performance Molecular Simulations Through Multi-Level Parallelism from Laptops to Supercomputers. *SoftwareX* **2015**, *1-2*, 19-25.
- 45. Pedone, A.; Malavasi, G.; Menziani, M. C.; Cormack, A. N.; Segre, U., A New Self-Consistent Empirical Interatomic Potential Model for Oxides, Silicates, and Silica-Based Glasses. *J. Phys. Chem. B* **2006**, *110*, 11780-11795.
- 46. Curtarolo, S.; Setyawan, W.; Wang, S.; Xue, J.; Yang, K.; Taylor, R. H.; Nelson, L. J.; Hart, G. L. W.; Sanvito, S.; Buongiorno-Nardelli, M.; Mingo, N.; Levy, O., AFLOWLIB.ORG: A Distributed Materials

- Properties Repository from High-Throughput Ab-Initio Calculations. *Comput. Mater. Sci.* **2012,** *58,* 227-235.
- 47. Mishra, R. K.; Mohamed, A. K.; Geissbühler, D.; Manzano, H.; Jamil, T.; Shahsavari, R.; Kalinichev, A. G.; Galmarini, S.; Tao, L.; Heinz, H.; Pellenq, R.; Van Duin, A. C.; Parker, S. C.; Flatt, R. J.; Bowen, P., CEMFF: A Force Field Database for Cementitious Materials Including Validations, Applications and Opportunities. *Cem. Concr. Res.* **2017**, *102*, 68-89.
- 48. Jain, A.; Hautier, G.; Moore, C. J.; Ong, S. P.; Fischer, C. C.; Mueller, T.; Persson, K. A.; Ceder, G., A High-Throughput Infrastructure for Density Functional Theory Calculations. *Comput. Mater. Sci.* **2011**, *50*, 2295-2310.
- 49. Senftle, T. P.; Hong, S.; Islam, M. M.; Kylasa, S. B.; Zheng, Y.; Shin, Y. K.; Junkermeier, C.; Engel-Herbert, R.; Janik, M. J.; Aktulga, H. M., The ReaxFF Reactive Force-Field: Development, Applications and Future Directions. *npj Comput. Mater.* **2016**, *2*, 1-14.
- 50. Chenoweth, K.; van Duin, A. C. T.; Goddard, W. A., ReaxFF Reactive Force Field for Molecular Dynamics Simulations of Hydrocarbon Oxidation. *J. Phys. Chem. A* **2008**, *112*, 1040-1053.
- 51. Cygan, R. T.; Liang, J.-J.; Kalinichev, A. G., Molecular Models of Hydroxide, Oxyhydroxide, and Clay Phases and the Development of a General Force Field. *J. Phys. Chem. B.* **2004**, *108*, 1255-1266.
- 52. Cygan, R. T.; Greathouse, J. A.; Kalinichev, A. G., Advances in Clayff Molecular Simulation of Layered and Nanoporous Materials and Their Aqueous Interfaces. *J. Phys. Chem. C* **2021**, *125*, 17573-17589.
- 53. Rappé, A. K.; Casewit, C. J.; Colwell, K.; Goddard III, W. A.; Skiff, W. M., UFF, a Full Periodic Table Force Field for Molecular Mechanics and Molecular Dynamics Simulations. *J. Am. Chem. Soc.* **1992,** *114,* 10024-10035.
- 54. Elliott, R. S.; Tadmor, E. B., *Open Knowledgebase of Interatomic Models (OpenKIM), an Application Programming Interface (API)*. https://openkim.org, 2011-2023.
- 55. Tadmor, E. B.; Elliott, R. S.; Sethna, J. P.; Miller, R. E.; Becker, C. A., The Potential of Atomistic Simulations and the Knowledgebase of Interatomic Models. *Jom* **2011**, *63*, 17-17.
- 56. Wang, S.; Zhu, E.; Huang, Y.; Heinz, H., Direct Correlation of Oxygen Adsorption on Platinum-Electrolyte Interfaces with the Activity in the Oxygen Reduction Reaction. *Sci. Adv.* **2021**, *7*, eabb1435.
- 57. Geada, I. L.; Ramezani-Dakhel, H.; Jamil, T.; Sulpizi, M.; Heinz, H., Insight into Induced Charges at Metal Surfaces and Biointerfaces Using a Polarizable Lennard-Jones Potential. *Nat. Comm.* **2018**, *9*, 716.
- 58. Choi, Y. K.; Kern, N. R.; Kim, S.; Kanhaiya, K.; Afshar, Y.; Jeon, S. H.; Jo, S.; Brooks, B. R.; Lee, J.; Tadmor, E. B.; Heinz, H.; Im, W., CHARMM-GUI Nanomaterial Modeler for Modeling and Simulation of Nanomaterial Systems. *J. Chem. Theor. Comput.* **2022**, *18*, 479-493.
- 59. Mark, L. O.; Zhu, C.; Medlin, J. W.; Heinz, H., Understanding the Surface Reactivity of Ligand-Protected Metal Nanoparticles for Biomass Upgrading. *ACS Catal.* **2020**, *10*, 5462-5474.
- 60. Heinz, H.; Koerner, H.; Anderson, K. L.; Vaia, R. A.; Farmer, B. L., Force Field for Mica-Type Silicates and Dynamics of Octadecylammonium Chains Grafted to Montmorillonite. *Chem. Mater.* **2005**, *17*, 5658-5669.
- 61. Psofogiannakis, G. M.; McCleerey, J. F.; Jaramillo, E.; van Duin, A. C., ReaxFF Reactive Molecular Dynamics Simulation of the Hydration of Cu-SSZ-13 Zeolite and the Formation of Cu Dimers. *J. Phys. Chem. C* **2015**, *119*, 6678-6686.
- 62. Shin, Y. K.; Kwak, H.; Vasenkov, A. V.; Sengupta, D.; Van Duin, A. C., Development of a ReaxFF Reactive Force Field for Fe/Cr/O/S and Application to Oxidation of Butane over a Pyrite-Covered Cr₂O₃ Catalyst. *ACS Catal.* **2015**, *5*, 7226-7236.
- 63. Liu, S.-S.; Saha, L. C.; Iskandarov, A.; Ishimoto, T.; Yamamoto, T.; Umeno, Y.; Matsumura, S.; Koyama, M., Atomic Structure Observations and Reaction Dynamics Simulations on Triple Phase Boundaries in Solid-Oxide Fuel Cells. *Commun. Chem.* **2019**, *2*, 1-9.

- 64. Zhang, Q.; Çağın, T.; Van Duin, A.; Goddard III, W. A.; Qi, Y.; Hector Jr, L. G., Adhesion and Nonwetting-Wetting Transition in the Al/α-Al₂O₃ Interface. *Phys. Rev. B* **2004**, *69*, 045423.
- 65. Valero, R.; Gomes, J. R.; Truhlar, D. G.; Illas, F., Density Functional Study of CO and NO Adsorption on Ni-Doped MgO(100). *J. Chem. Phys.* **2010**, *132*, 104701.
- 66. Alessio, M.; Usvyat, D.; Sauer, J., Chemically Accurate Adsorption Energies: CO and H2O on the MgO(001) Surface. *J. Chem. Theor. Comput.* **2019**, *15*, 1329-1344.
- 67. CRC Handbook of Chemistry and Physics. 101st ed.; CRC Press: Boca Raton, FL, 2020.
- 68. Mishra, R. K.; Fernández-Carrasco, L.; Flatt, R. J.; Heinz, H., A Force Field for Tricalcium Aluminate to Characterize Surface Properties, Initial Hydration, and Organically Modified Interfaces in Atomic Resolution. *Dalton Trans.* **2014**, *43*, 10602-10616.
- 69. Belokoneva, E.; Shcherbakova, Y. K., Electron Density in Synthetic Escolaite Cr₂O₃ with a Corundum Structure and its Relation to Antiferromagnetic Properties. *Russ. J. Inorg. Chem.* **2003**, *48*, 861-869.
- 70. Thong, N.; Schwarzenbach, D., The Use of Electric Field Gradient Calculations in Charge Density Refinements. II. Charge Density Refinement of the Low-Quartz Structure of Aluminum Phosphate. *Acta Cryst. A* **1979**, *35*, 658-664.
- 71. Batsanov, S. S., Van der Waals Radii of Elements. *Inorg. Mater.* **2001,** *37*, 871-885.
- 72. Liu, H.; Espe, M.; Modarelli, D. A.; Arias, E.; Moggio, I.; Ziolo, R. F.; Heinz, H., Interaction of Substituted Poly (phenyleneethynylene) s with Ligand-Stabilized CdS Nanoparticles. *J. Mater. Chem. A* **2014**, *2*, 8705-8711.
- 73. Hall, D. S.; Lockwood, D. J.; Bock, C.; MacDougall, B. R., Nickel Hydroxides and Related Materials: a Review of Their Structures, Synthesis and Properties. *Proc. R. Soc. A: Math. Phys. Eng. Sci.* **2015**, *471*, 20140792.
- 74. Ekbundit, S.; Leinenweber, K.; Yarger, J.; Robinson, J.; Verhelst-Voorhees, M.; Wolf, G., New High-Pressure Phase and Pressure-Induced Amorphization of Ca(OH)₂: Grain Size Effect. *J. Solid State Chem.* **1996**, *126*, 300-307.
- 75. Downs, R. T.; Hall-Wallace, M., The American Mineralogist Crystal Structure Database. *Am. Mineral.* **2003**, *88*, 247-250.
- 76. Curtarolo, S.; Setyawan, W.; Hart, G. L. W.; Jahnatek, M.; Chepulskii, R. V.; Taylor, R. H.; Wanga, S. D.; Xue, J. K.; Yang, K. S.; Levy, O.; Mehl, M. J.; Stokes, H. T.; Demchenko, D. O.; Morgan, D., AFLOW: An Automatic Framework for High-Throughput Materials Discovery. *Comput. Mater. Sci.* **2012**, *58*, 218-226.
- 77. Fiquet, G.; Richet, P.; Montagnac, G., High-Temperature Thermal Expansion of Lime, Periclase, Corundum and Spinel. *Phys. Chem. Miner.* **1999,** *27*, 103-111.
- 78. Cairns, R.; Ott, E., X-Ray Studies of the System Nickel—Oxygen—Water. I. Nickelous Oxide and Hydroxide¹. *J. Am. Chem. Soc.* **1933**, *55*, 527-533.
- 79. Smith, N., The Structure of Thin Films of Metallic Oxides and Hydrates. *J. Am. Chem. Soc.* **1936**, *58*, 173-179.
- 80. Henderson, D.; Gutowsky, H., A Nuclear Magnetic Resonance Determination of the Hydrogen Positions in Ca(OH)₂. *Am. Mineral.: J. Earth Planet. Mater.* **1962**, *47*, 1231-1251.
- 81. Busing, W. R.; Levy, H. A., Neutron Diffraction Study of Calcium Hydroxide. *J. Chem. Phys.* **1957**, *26*, 563-568.
- 82. Desgranges, L.; Grebille, D.; Calvarin, G.; Chevrier, G.; Floquet, N.; Niepce, J.-C., Hydrogen Thermal Motion in Calcium Hydroxide: Ca(OH)₂. *Acta Crystallogr., Sect. B: Struct. Sci.* **1993**, *49*, 812-817.
- 83. Catti, M.; Ferraris, G.; Hull, S.; Pavese, A., Static Compression and H Disorder in Brucite, Mg(OH)₂, to 11 GPa: a Powder Neutron Diffraction Study. *Phys. Chem. Miner.* **1995**, *22*, 200-206.
- 84. Fu, Y. T.; Heinz, H., Cleavage Energy of Alkylammonium-Modified Montmorillonite and Relation to Exfoliation in Nanocomposites: Influence of Cation Density, Head Group Structure, and Chain Length. *Chem. Mater.* **2010**, *22*, 1595-1605.

- 85. Mishra, R. K.; Flatt, R. J.; Heinz, H., Force Field for Tricalcium Silicate and Insight into Nanoscale Properties: Cleavage, Initial Hydration, and Adsorption of Organic Molecules. *J. Phys. Chem. C* **2013**, *117*, 10417-10432.
- 86. Dhakane, A.; Varshney, V.; Liu, J.; Heinz, H.; Jain, A., Molecular Dynamics Simulations of Separator-Cathode Interfacial Thermal Transport in a Li-ion Cell. *Surf. Interfaces* **2020**, *21*, 100674.
- 87. Zhao, Y.; Truhlar, D., The M06 Suite of Density Functionals for Main Group Thermochemistry, Thermochemical Kinetics, Noncovalent Interactions, Excited States, and Transition Elements: Two New Functionals and Systematic Testing of Four M06-class Functionals and 12 Other Functionals. *Theor. Chem. Acc.* **2008**, *120*, 215-241.
- 88. Wang, Y.; Verma, P.; Jin, X.; Truhlar, D. G.; He, X., Revised M06 Density Functional for Main-Group and Transition-Metal Chemistry. *Proc. Natl. Acad. Sci. U. S. A.* **2018**, *115*, 10257-10262.
- 89. Yu, H. Y. S.; He, X.; Li, S. H. L.; Truhlar, D. G., MN15: A Kohn-Sham Global-Hybrid Exchange-Correlation Density Functional with Broad Accuracy for Multi-Reference and Single-Reference Systems and Noncovalent Interactions. *Chem. Sci.* **2016**, *7*, 5032-5051.
- 90. Liu, W.; Tkatchenko, A.; Scheffler, M., Modeling Adsorption and Reactions of Organic Molecules at Metal Surfaces. *Acc. Chem. Res.* **2014**, *47*, 3369-3377.
- 91. Ruiz, V. G.; Liu, W.; Zojer, E.; Scheffler, M.; Tkatchenko, A., Density-Functional Theory with Screened van der Waals Interactions for the Modeling of Hybrid Inorganic-Organic Systems. *Phys. Rev. Lett.* **2012**, *108*, 146103.
- 92. Goerigk, L.; Grimme, S., A Thorough Benchmark of Density Functional Methods for General Main Group Thermochemistry, Kinetics, and Noncovalent Interactions. *Phys. Chem. Chem. Phys.* **2011**, *13*, 6670-6688.
- 93. Ruiz, V. G.; Liu, W.; Tkatchenko, A., Density-Functional Theory with Screened van der Waals Interactions Applied to Atomic and Molecular Adsorbates on Close-Packed and Non-Close-Packed Surfaces. *Phys. Rev. B* **2016**, *93*, 035118.
- 94. Drazin, J. W.; Castro, R. H., Water Adsorption Microcalorimetry Model: Deciphering Surface Energies and Water Chemical Potentials of Nanocrystalline Oxides. *J. Phys. Chem. C* **2014**, *118*, 10131-10142.
- 95. McHale, J.; Navrotsky, A.; Perrotta, A., Effects of Increased Surface Area and Chemisorbed H_2O on the Relative Stability of Nanocrystalline γ -Al₂O₃ and α -Al₂O₃. *J. Phys. Chem. B* **1997**, *101*, 603-613.
- 96. Mazeina, L.; Navrotsky, A., Enthalpy of Water Adsorption and Surface Enthalpy of Goethite (α -FeOOH) and Hematite (α -Fe₂O₃). *Chem. Mater.* **2007**, *19*, 825-833.
- 97. Navrotsky, A.; Mazeina, L.; Majzlan, J., Size-Driven Structural and Thermodynamic Complexity in Iron Oxides. *Science* **2008**, *319*, 1635-1638.
- 98. Jura, G.; Garland, C. W., The Experimental Determination of the Surface Tension of Magnesium Oxide. *J. Am. Chem. Soc.* **1952**, *74*, 6033-6034.
- 99. Westwood, A.; Goldheim, D., Cleavage Surface Energy of {100} Magnesium Oxide. *J. Appl. Phys.* **1963,** *34*, 3335-3339.
- 100. Paras, J.; Takeda, O.; Wu, M.; Allanore, A., The Surface Tension and Density of Molten Sc2O3, La2O3, Y2O3, Al2O3, and MgO Measured via a Pendant Droplet Method. *Metallurg. Mater. Trans. B* **2022**, *53*, 2077-2087.
- 101. Zadumkin, S. N.; Khulamkhanov, V. K., The Surface Energy of Certain Oxides, Sulfides, and Selenides. *Izv. Vys. Ucheb. Zav., Fiz.* **1962**, *4*, 112-114.
- 102. Muhmood, L.; Wegener, M.; Sun, S.; Deev, A. Control of Molten CaO Al2O3 Oxide Jets with Focus on Thermophysical Property Measurements and Some Limitations, In Advances in Molten Slags, Fluxes, and Salts: Proceedings of the 10th International Conference on Molten Slags, Fluxes and Salts 2016, Cham, 2016; Reddy, R. G.; Chaubal, P.; Pistorius, P. C.; Pal, U., Eds., Springer International Publishing: Cham, 2016; pp 547-555.

- 103. Tyson, W. R.; Miller, W. A., Surface Free-Energies of Solid Metals Estimation from Liquid Surface-Tension Measurements. *Surf. Sci.* **1977**, *62*, 267-276.
- 104. Brunauer, S.; Kantro, D. L.; Weise, C. H., The Surface Energies of Calcium Oxide and Calcium Hydroxide. *Can. J. Chem.* **1956**, *34*, 729-742.
- 105. Wiederhorn, S. M.; Moses, R. L.; Bean, B. L., Plastic Deformation and Fracture Surface Energy of Sodium Chloride. *J. Am. Ceram. Soc.* **1970**, *53*, 18-23.
- 106. Marcus, Y., Surface Tension and Cohesive Energy Density of Molten Salts. *Thermochim. Acta* **2013**, *571*, 77-81.
- 107. Ayyad, A. H., On the Surface Tension of Molten Salts and its Temperature Dependence. *Phys. Chem. Liquids* **2017**, *55*, 120-130.
- 108. Igarashi, K.; Iwadate, Y.; Mochinaga, J., Surface Tensions of Molten Binary CaCl2-NaCl, LaCl3-NaCl, and LaCl3-CaCl2 and Ternary LaCl3-CaCl2-NaCl Systems. *Z. Naturforsch.*, *A: Phys. Sci.* **1987**, *42*, 853-857.
- 109. McHale, J.; Auroux, A.; Perrotta, A.; Navrotsky, A., Surface Energies and Thermodynamic Phase Stability in Nanocrystalline Aluminas. *Science* **1997**, *277*, 788-791.
- 110. Navrotsky, A., Energetics of Nanoparticle Oxides: Interplay Between Surface Energy and Polymorphism. *Geochem. Trans.* **2003**, *4*, 34.
- 111. Brunauer, S.; Kantro, D.; Weise, C., The Surface Energies of Calcium Oxide and Calcium Hydroxide. *Can. J. Chem.* **1956**, *34*, 729-742.
- 112. Heinz, H.; Vaia, R. A.; Farmer, B. L.; Naik, R. R., Accurate Simulation of Surfaces and Interfaces of Face-Centered Cubic Metals Using 12–6 and 9–6 Lennard-Jones Potentials. *J. Phys. Chem. C* **2008**, *112*, 17281-17290.
- 113. Li, A.; Kong, S.; Guo, C.; Ooka, H.; Adachi, K.; Hashizume, D.; Jiang, Q.; Han, H.; Xiao, J.; Nakamura, R., Enhancing the Stability of Cobalt Spinel Oxide Towards Sustainable Oxygen Evolution in Acid. *Nat. Catal.* **2022**, *5*, 109-118.
- 114. Finger, L. W.; Hazen, R. M.; Hofmeister, A. M., High-Pressure Crystal Chemistry of Spinel (MgAl₂O₄) and magnetite (Fe₃O₄): Comparisons with Silicate Spinels. *Phys. Chem. Miner.* **1986,** *13*, 215-220.
- 115. Ganesh, I., A Review on Magnesium Aluminate (MgAl₂O₄) Spinel: Synthesis, Processing and Applications. *Int. Mater. Rev.* **2013**, *58*, 63-112.
- 116. Atkinson, A., Transport Processes During the Growth of Oxide Films at Elevated Temperature. *Rev. Mod. Phys.* **1985**, *57*, 437.
- 117. Yu, J.; Rosso, K. M.; Bruemmer, S. M., Charge and Ion Transport in NiO and Aspects of Ni Oxidation from First Principles. *J. Phys. Chem. C* **2012**, *116*, 1948-1954.
- 118. Haugsrud, R.; Norby, T., Determination of Thermodynamics and Kinetics of Point Defects in NiO Using the Rosenburg Method. *Solid State Ionics* **1998**, *111*, 323-332.
- 119. Atkinson, A.; Taylor, R., The Diffusion of ⁶³Ni Along Grain Boundaries in Nickel Oxide. *Philos. Mag. A* **1981**, *43*, 979-998.
- 120. Gupta, Y.; Weirick, L., Self-Diffusion of Calcium in Single Crystal Calcium Oxide. *J. Phys. Chem. Solids* **1967**, *28*, 811-821.
- 121. Kumar, V.; Gupta, Y., Cation Self-Diffusion in Single Crystal CaO. *J. Phys. Chem. Solids* **1969,** *30,* 677-685.
- 122. Huang, J.; MacKerell, A. D., CHARMM36 All-Atom Additive Protein Force Field: Validation Based on Comparison to NMR Data. *J. Comput. Chem.* **2013**, *34*, 2135-2145.
- 123. Karalti, O.; Alfè, D.; Gillan, M. J.; Jordan, K. D., Adsorption of a Water Molecule on the MgO(100) Surface as Described by Cluster and Slab Models. *Phys. Chem. Chem. Phys.* **2012**, *14*, 7846-7853.
- 124. Ferry, D.; Glebov, A.; Senz, V.; Suzanne, J.; Toennies, J. P.; Weiss, H., The Properties of a Two-Dimensional Water Layer on MgO (001). *Surf. Sci.* **1997**, *377-379*, 634-638.

- 125. Ferry, D.; Picaud, S.; Hoang, P. N. M.; Girardet, C.; Giordano, L.; Demirdjian, B.; Suzanne, J., Water Monolayers on MgO(100): Structural Investigations by LEED Experiments, Tensor LEED Dynamical Analysis and Potential Calculations. *Surf. Sci.* **1998**, *409*, 101-116.
- 126. Ding, Z.; Selloni, A., Hydration Structure of Flat and Stepped MgO Surfaces. *J. Chem. Phys.* **2021**, *154*, 114708.
- 127. Kim, Y. D.; Stultz, J.; Goodman, D. W., Dissociation of Water on MgO(100). *J. Phys. Chem. B* **2002**, *106*, 1515-1517.
- 128. Yu, Y.; Guo, Q.; Liu, S.; Wang, E.; Møller, P. J., Partial Dissociation of Water on a MgO(100) Film. *Phys. Rev. B* **2003**, *68*, 115414.
- 129. Huang, L.; Yang, Z.; Wang, S., Influence of Calcination Temperature on the Structure and Hydration of MgO. *Constr. Building Mater.* **2020**, *262*, 120776.
- 130. Thomas, J. J.; Musso, S.; Prestini, I., Kinetics and Activation Energy of Magnesium Oxide Hydration. *J. Am. Ceram. Soc.* **2014**, *97*, 275-282.
- 131. Tait, S. L.; Dohnálek, Z.; Campbell, C. T.; Kay, B. D., n-Alkanes on MgO (100). II. Chain Length Dependence of Kinetic Desorption Parameters for Small n-Alkanes. *J. Chem. Phys.* **2005**, *122*, 164708.
- 132. Sellers, J. R. V. Adsorption and Thin-Film Adhesion on Single-Crystalline Surfaces: Enthalpies, Entropies, and Kinetic Prefactors for Surface Reactions. 2014.
- 133. Santra, G.; Sylvetsky, N.; Martin, J. M. L., Minimally Empirical Double-Hybrid Functionals Trained against the GMTKN55 Database: revDSD-PBEP86-D4, revDOD-PBE-D4, and DOD-SCAN-D4. *J. Phys. Chem. A* **2019**, *123*, 5129-5143.
- 134. Montemore, M. M.; van Spronsen, M. A.; Madix, R. J.; Friend, C. M., O2 Activation by Metal Surfaces: Implications for Bonding and Reactivity on Heterogeneous Catalysts. *Chem. Rev.* **2018**, *118*, 2816-2862.
- 135. Zhu, C.; Hoff, S. E.; Hémadi, M.; Heinz, H., Accurate and Ultrafast Simulation of Molecular Recognition and Assembly on Metal Surfaces in Four Dimensions. *Acs Nano* **2023**, *17*, 9938-9952.
- 136. Wang, S.; Hou, K.; Heinz, H., Accurate Compatible Force Fields for Molecular Oxygen, Nitrogen and Hydrogen to Simulate Heterogeneous Electrolytes and Interfaces. *J. Chem. Theor. Comput.* **2021**, *17*, 5198-5213.
- 137. Hoff, S. E.; Liu, J.; Heinz, H., Binding Mechanism and Binding Free Energy of Amino Acids and Citrate to Hydroxyapatite Surfaces as a Function of Crystallographic Facet, pH, and Electrolytes. *J. Colloid Interface Sci.* **2022**, *605*, 685-700.
- 138. Akkineni, S.; Zhu, C.; Chen, J.; Song, M.; Hoff Samuel, E.; Bonde, J.; Tao, J.; Heinz, H.; Habelitz, S.; De Yoreo James, J., Amyloid-like Amelogenin Nanoribbons Template Mineralization via a Low-energy Interface of Ion Binding Sites. *Proc. Natl. Acad. Sci. U. S. A.* **2022**, *119*, e2106965119.
- 139. Seker, U. O. S.; Demir, H. V., Material Binding Peptides for Nanotechnology. *Molecules* **2011**, *16*, 1426-1451.
- 140. Lower, B. H.; Lins, R. D.; Oestreicher, Z.; Straatsma, T. P.; Hochella, M. F., Jr.; Shi, L.; Lower, S. K., In Vitro Evolution of a Peptide with a Hematite Binding Motif That May Constitute a Natural Metal-Oxide Binding Archetype. *Environ. Sci. Technol.* **2008**, *42*, 3821-3827.
- 141. Kasprzyk-Hordern, B., Chemistry of Alumina, Reactions in Aqueous Solution and its Application in Water Treatment. *Adv. Colloid Interface Sci.* **2004**, *110*, 19-48.
- 142. Sung, J.; Zhang, L.; Tian, C.; Shen, Y. R.; Waychunas, G. A., Effect of pH on the Water/ α -Al2O3 (1T02) Interface Structure Studied by Sum-Frequency Vibrational Spectroscopy. *J. Phys. Chem. C* **2011**, 115, 13887-13893.
- 143. Lee, S. Y.; Welbourn, R.; Clarke, S. M.; Skoda, M. W. A.; Clifton, L.; Zarbakhsh, A., Adsorption of Sodium Hexanoate on α-Alumina. *J. Colloid Interface Sci.* **2013**, *407*, 348-353.
- 144. Parks, G. A., Surface and Interfacial Free Energies of Quartz. *J. Geophys. Res.* **1984**, *89* (B6), 3997-4008.

- 145. Brace, W. F.; Walsh, J. B., Some Direct Measurements of Surface Energy of Quartz and Orthoclase. *Am. Miner.* **1962**, *47*, 1111-1122.
- 146. Pabst, W.; Gregorova, E., Elastic Properties of Silica Polymorphs. *Ceramics-Silikaty* **2013**, *57*, 167-184.
- 147. Phillips, J. C.; Braun, R.; Wang, W.; Gumbart, J.; Tajkhorshid, E.; Villa, E.; Chipot, C.; Skeel, R. D.; Kale, L.; Schulten, K., Scalable Molecular Dynamics with NAMD. *J. Comput. Chem.* **2005**, *26*, 1781-1802.
- 148. Case, D. A.; Cheatham Iii, T. E.; Darden, T.; Gohlke, H.; Luo, R.; Merz Jr, K. M.; Onufriev, A.; Simmerling, C.; Wang, B.; Woods, R. J., The Amber Biomolecular Simulation Programs. *J. Comput. Chem.* **2005**, *26*, 1668-1688.
- 149. Peter Eastman, J. S., John D. Chodera, Robert T. McGibbon, Yutong Zhao, Kyle A. Beauchamp, Lee-Ping Wang, Andrew C. Simmonett, Matthew P. Harrigan, Chaya D. Stern, Rafal P. Wiewiora, Bernard R. Brooks, Vijay S. Pande, OpenMM 7: Rapid Development of High Performance Algorithms for Molecular Dynamics. *PLOS Comput. Biol.* **2017**, 1005659.
- 150. Brooks, B. R.; Brooks Iii, C. L.; Mackerell Jr, A. D.; Nilsson, L.; Petrella, R. J.; Roux, B.; Won, Y.; Archontis, G.; Bartels, C.; Boresch, S.; Caflisch, A.; Caves, L.; Cui, Q.; Dinner, A. R.; Feig, M.; Fischer, S.; Gao, J.; Hodoscek, M.; Im, W.; Kuczera, K.; Lazaridis, T.; Ma, J.; Ovchinnikov, V.; Paci, E.; Pastor, R. W.; Post, C. B.; Pu, J. Z.; Schaefer, M.; Tidor, B.; Venable, R. M.; Woodcock, H. L.; Wu, X.; Yang, W.; York, D. M.; Karplus, M., CHARMM: The Biomolecular Simulation Program. *J. Comput. Chem.* **2009**, *30*, 1545-1614.
- 151. Jung, J.; Mori, T.; Kobayashi, C.; Matsunaga, Y.; Yoda, T.; Feig, M.; Sugita, Y., GENESIS: A Hybrid-Parallel and Multi-Scale Molecular Dynamics Simulator with Enhanced Sampling Algorithms for Biomolecular and Cellular Simulations. *WIREs Computational Molecular Science* **2015**, *5*, 310-323.
- 152. Plimpton, S., Fast Parallel Algorithms for Short-Range Molecular Dynamics. *J. Comput. Phys.* **1995**, *117*, 1-19.
- 153. Pedone, A., Properties Calculations of Silica-Based Glasses by Atomistic Simulations Techniques: A Review. *J. Phys. Chem. C* **2009**, *113*, 20773-20784.
- 154. Ramezani-Dakhel, H.; Bedford, N. M.; Woehl, T. J.; Knecht, M. R.; Naik, R. R.; Heinz, H., Nature of Peptide Wrapping onto Metal Nanoparticle Catalysts and Driving Forces for Size Control. *Nanoscale* **2017**, *9*, 8401-8409.
- 155. Bedford, N. M.; Ramezani-Dakhel, H.; Slocik, J. M.; Briggs, B. D.; Ren, Y.; Frenkel, A. I.; Petkov, V.; Heinz, H.; Naik, R. R.; Knecht, M. R., Elucidation of Peptide-Directed Palladium Surface Structure for Biologically Tunable Nanocatalysts. *Acs Nano* **2015**, *9*, 5082-5092.
- 156. Ramezani-Dakhel, H.; Mirau, P. A.; Naik, R. R.; Knecht, M. R.; Heinz, H., Stability, Surface Features, and Atom Leaching of Palladium Nanoparticles: Toward Prediction of Catalytic Functionality. *Phys. Chem. Phys.* **2013**, *15*, 5488-5492.
- 157. Frankel, G. S.; Vienna, J. D.; Lian, J.; Scully, J. R.; Gin, S.; Ryan, J. V.; Wang, J.; Kim, S. H.; Windl, W.; Du, J., A Comparative Review of the Aqueous Corrosion of Glasses, Crystalline Ceramics, and Metals. *npj Materials Degradation* **2018**, *2*, 15.
- 158. Cabot, A.; Puntes, V. F.; Shevchenko, E.; Yin, Y.; Balcells, L.; Marcus, M. A.; Hughes, S. M.; Alivisatos, A. P., Vacancy Coalescence during Oxidation of Iron Nanoparticles. *J. Am. Chem. Soc.* **2007**, *129*, 10358-10360.
- 159. Steele, B. C. H., Oxygen Transport and Exchange in Oxide Ceramics. *J. Power Sources* **1994,** *49*, 1-14.
- 160. Kear, G.; Barker, B. D.; Walsh, F. C., Electrochemical Corrosion of Unalloyed Copper in Chloride Media—A Critical Review. *Corrosion Sci.* **2004**, *46*, 109-135.
- 161. Chen, B. W. J.; Xu, L.; Mavrikakis, M., Computational Methods in Heterogeneous Catalysis. *Chem. Rev.* **2021**, *121*, 1007-1048.

- 162. Sengul, M. Y.; Song, Y.; Nayir, N.; Gao, Y. W.; Hung, Y.; Dasgupta, T.; van Duin, A. C. T., INDEEDopt: a Deep Learning-Based ReaxFF Parameterization Framework. *NPJ Comput. Mater.* **2021,** *7*, 68.
- 163. Doerr, S.; Majewski, M.; Pérez, A.; Krämer, A.; Clementi, C.; Noe, F.; Giorgino, T.; Fabritiis, G. D., TorchMD: A Deep Learning Framework for Molecular Simulations. *J. Chem. Theor. Comp.* **2021**, *17*, 2355-2363.
- 164. Chmiela, S.; Vassilev-Galindo, V.; Unke, O. T.; Kabylda, A.; Sauceda, H. E.; Tkatchenko, A.; Müller, K.-R., Accurate Global Machine Learning Force Fields for Molecules with Hundreds of Atoms. *Sci. Adv.* **2023,** *9*, eadf0873.
- 165. Scherer, C.; Scheid, R.; Andrienko, D.; Bereau, T., Kernel-Based Machine Learning for Efficient Simulations of Molecular Liquids. *J. Chem. Theor. Comput.* **2020**, *16*, 3194-3204.
- 166. Noé, F.; Tkatchenko, A.; Müller, K.-R.; Clementi, C., Machine Learning for Molecular Simulation. *Ann. Rev. Phys. Chem.* **2020**, *71*, 361-390.
- 167. Schleder, G. R.; Padilha, A. C. M.; Acosta, C. M.; Costa, M.; Fazzio, A., From DFT to Machine Learning: Recent Approaches to Materials Science-A Review. *J. Physics: Materials* **2019**, *2*, 032001.
- 168. Winetrout, J. J.; Kanhaiya, K.; Sachdeva, G.; Pandey, R.; Damirchi, B.; Duin, A. v.; Odegard, G. M.; Heinz, H., Implementing Reactivity in Molecular Dynamics Simulations with the Interface Force Field (IFF-R) and Other Harmonic Force Fields. *ArXiv preprint* **2021**, arXiv:2107.14418.
- 169. Heinz, H.; Vaia, R. A.; Koerner, H.; Farmer, B. L., Photoisomerization of Azobenzene Grafted to Layered Silicates: Simulation and Experimental Challenges. *Chem. Mater.* **2008**, *20*, 6444-6456.
- 170. *Materials Studio 7 Program Suite and User Guide*. Biovia/Dassault Systemes: Cambridge, UK, 2015-2019.

Table of Contents Graphic

